creative commons
COMMONS DEED

저작자표시-비영리-변경금지 2.0 대한민국

이용자는 아래의 조건을 따르는 경우에 한하여 자유롭게

- 이 저작물을 복제, 배포, 전송, 전시, 공연 및 방송할 수 있습니다.

다음과 같은 조건을 따라야 합니다:

저작자표시. 귀하는 원저작자를 표시하여야 합니다.

비영리. 귀하는 이 저작물을 영리 목적으로 이용할 수 없습니다.

변경금지. 귀하는 이 저작물을 개작, 변형 또는 가공할 수 없습니다.

- 귀하는, 이 저작물의 재이용이나 배포의 경우, 이 저작물에 적용된 이용허락조건을 명확하게 나타내어야 합니다.
- 저작권자로부터 별도의 허가를 받으면 이러한 조건들은 적용되지 않습니다.

저작권법에 따른 이용자의 권리는 위의 내용에 의하여 영향을 받지 않습니다.

이것은 이용허락규약(Legal Code)을 이해하기 쉽게 요약한 것입니다.

Disclaimer

dCollection

[UCI]I804:48009-200000370129

이학석사 학위논문

리튬이차전지의 양극소재로 사용되는 붕산염기반의 Fe, Mn 과 Co 복합소재의 합성과 구조적 연구

Synthesis and structural studies of borate based Mn, Fe and Co complex as a cathode material for Li–ion

울산대학교 대학원

화학과

이인영

Synthesis and structural studies of borate based Mn, Fe and Co complex as a cathode material for Li–ion

지도교수 이 영 일

이 논문을 이학석사학위 논문으로 제출함

2021년 02월

울산대학교 대학원

화학과

이 인 영

이인영의 석사학위 논문을 인준함

심사위원 이영일 (인)

심사위원 류광선 (인)

심사위원 이승구 (인)

울산대학교대학원

2021년 02월

Abstract

Polyanionic structured compounds are widely studied as a cathode material for lithium-ion battery (LIB). Among them, lithium metal borate ($LiMBO_3$, M = Mn, Fe, and Co) form has the lowest weight, thus offering the highest theoretical capacity (220 mAhg $^{-1}$) and providing an advantage of safety. Also, the energy density is expected to be higher than lithium metal phosphate. Among borate-based materials, $LiMnBO_3$ has the highest operating potential, while $LiFeBO_3$ has the highest theoretical capacity. On the other hand, $LiCoBO_3$ has an excellent theoretical capacity (215 mAh g^{-1}) and 4 V operating potential. $LiMBO_3$ (M = Mn, Fe, Co) compounds are crystallized in the monoclinic space group C2/c. In this study, $LiFe_{1-x}Mn_xBO_3$ and $LiFe_{1-x}Co_xBO_3$ (x = 0, 0.25, 0.5, 0.75, and 1.0) composite materials have been synthesized with solid-state reaction method for structural studies according to the amount of d-electrons on metal sites. The morphological and structural studies of synthesized materials have been identified with X-ray diffraction (XRD) and ^{7}Li nuclear magnetic resonance (NMR). Also, quantitative analysis for the ratio of metal has been performed with laser-induced breakdown spectroscopy (LIBS).

Contents

Abstract 1

List of tables 4

List of figures 4

1. Introduction of lithium-ion battery 8

1.1 Principle of lithium-ion battery 10

1.2 Cathode materials 14

1.3 Borate based cathode materials 17

1.3.1 Lithium iron borate ($LiFeBO_3$) 25

1.3.2 Lithium manganese borate ($LiMnBO_3$) 26

1.3.3 Lithium cobalt borate ($LiCoBO_3$) 27

2. Introduction of Nuclear Magnetic Resonance (NMR) 28

2.1 Principle of NMR 28

2.1.1 Boltzmann distribution 33

2.1.2 T_1 (Spin-lattice relaxation) and T_2 (Spin-spin relaxation) 34

2.2 Solid-state NMR 37

2.2.1 Magic Angle Spinning (MAS) technique 39

2.2.2 Spin echo pulse sequence (Hahn echo) 43

3. Experimental 46

3.1 Synthesis 46

3.1.1 Synthesis of $LiFe_{1-x}Mn_xBO_3$ (x = 0, 0.25, 0.5, 0.75) 47

3.1.1 Synthesis of $LiFe_{1-x}Co_xBO_3$ (x = 0, 0.25, 0.5, 0.75) 48

3.2 General characterization 51

3.3 Solid-state MAS NMR study of cathode materials 53

4. Results and Discussion 57

4.1 $LiFe_{1-x}Mn_xBO_3$ (x = 0, 0.25, 0.5, 0.75, 1.0) 57

4.1.1 X-ray Diffraction (XRD) 57

4.1.2 Laser-induced breakdown spectroscopy (LIBS) 60

4.1.3 ^{7}Li MAS NMR 64

4.1.4 Electrochemical study 69

4.2 $LiFe_{1-x}Co_xBO_3$ (x = 0, 0.25, 0.5, 0.75, 1.0) 72

4.2.1 X-ray Diffraction (XRD) 72

4.2.3 ^{7}Li MAS NMR 75

5. Conclusion 78

6. References 79

List of tables

Table 1. Calculated and experimental lattice parameters of $LiMBO_3$ (M = Mn, Fe, and Co). ΔV indicates volume change at delithiated $LiMBO_3$.[10]

Table 2. Electronic structures of Li_xMBO_3 (x = 1 and 0, M = Mn, Fe, and Co).[10]

Table 3. Normalization data of Mn and Fe, according to x value.

Table 4. Isotropic peak positions of the $LiFe_{1-x}Mn_xBO_3$.

Table 5. Isotropic peak positions of the $LiFe_{1-x}Co_xBO_3$.

List of figures

Figure 1.1 Ragone plot of various battery technologies with specification at the cell level for automotive applications.[1]

Figure 1.2 Charge and discharge mechanism of a lithium-ion battery.[4]

Figure 1.3 The energy diagram of electrode potential and electrolyte energy gap in the lithium-ion battery.[5]

Figure 1.4 Crystal structure of the three lithium-insertion compounds. The green balls represent Li^+.[9]

Figure 1.5 Monoclinic $LiM\,BO_3$ (M = Mn, Fe, Co) crystal structure along the (a) a-axis, (b) b-axis, and (c) c-axis.[14]

Figure 1.6 Edge-shared chains of LiO_4 parallel to the [001] direction.[10]

Figure 1.7 MO_5 trigonal bipyramid and schematic energy levels of the 3d bands of the TM ion.[10]

Figure 1.8 Scheme of energy levels and occupied electrons of $LiMBO_3$.

Figure 2.1 Distribution of nuclear spin (I) values for the major NMR active isotopes in the periodic table.[28]

Figure 2.2 The orientation of the nuclear magnet according to the presence of a magnetic field.

Figure 2.3 Zeeman Splitting of (a) a spin-½ nucleus under the magnetic field B_0 (b) Energy levels ($I > 0$).[26]

Figure 2.4 T_1 relaxation process.[30]

Figure 2.5 Transverse (T_2 and T_2*) relaxation processes.[30]

Figure 2.6 Comparison of ^{13}C NMR spectra in solution and solid-state.[31]

Figure 2.7 Representation of a MAS NMR probe head with an orientation of the stator at an angle (θ) of 54.7◦ between the axis of rotation and B_0.[33]

Figure 2.8 A schematic representation of a transient sedimentation NMR experiment. (a) An NMR magnet with a MAS probe. (b) Top: In a MAS probe, the NMR sample rotor is inclined at the 'magic angle' axis (54.73^o with respect to the static magnetic field B_0).[34]

Figure 2.9 Basic NMR pulse sequences: Hahn echo.[26]

Figure 2.10 The spin-echo: (a) Application of a 90° rf pulse at t = 0 tips the magnetization vector from its equilibrium state (green) into the x-y plane (dark blue); (b) In the x-y plane, spins at different locations lose phase coherence due to field inhomogeneity and begin to process at different frequencies, with faster spins shown in darker blue and slower spins in lighter blue. Application of a 180° rf pulse at t = τ rotates the magnetization about the y-axis; (c) The order of the spins is now reversed, with the slower spins 'ahead' of the faster spins; (d) this leads to the spins regaining coherence or 'refocusing' at a point in time t = 2τ.[26]

Figure 3.1 Solid-state synthetic procedures of $LiFe_{1-x}Mn_xBO_3$ as a cathode material.

Figure 3.2 Solid-state synthetic procedures of $LiFe_{1-x}Co_xBO_3$ as a cathode material.

Figure 3.3 Bruker Avance III 300MHz NMR.

Figure 3.4 2.5 and 4.0 mm sampling kit for solid-state NMR.

Figure 3.5 2.5 and 4.0 mm solid-state NMR rotors.[35]

Figure 4.1 The XRD patterns of $LiFe_{0.5}Mn_{0.5}BO_3$ sintered at various temperatures.

Figure 4.2 The XRD patterns of $LiFe_{1-x}Mn_xBO_3$ (x = 0, 0.25, 0.5, 0.75, 1.00) and an enlargement zone.

Figure 4.3 The Fe, Mn, and Co LIBS data for $LiFe_{1-x}Mn_xBO_3$ (x = 0, 0.25, 0.5, 0.75, 1.00)

Figure 4.4 Graphical representation of Table 3.

Figure 4.5 ^{7}Li MAS NMR spectra of $LiFe_{1-x}Mn_xBO_3$ at sample spinning rate of 30 kHz. The isotropic peaks are indicated by asterisk(*).

Figure 4.6 Graphical representation of Table 4 with linear fitting equation and coefficient of correlation.

Figure 4.7 Proposed energy splitting and filling of the trigonal bipyramidal crystal fields (e″, e′, and a1′).[14]

Figure 4.8 The long cycle ability at 0.5C of $LiFe_{1-x}Mn_xBO_3$ series.

Figure 4.9 The rate performance at various C-rate of $LiFe_{1-x}Mn_xBO_3$ series**.**

Figure 4.10 The XRD patterns of $LiFe_{0.75}Co_{0.25}BO_3$ sintered at various temperatures.

Figure 4.11 The XRD patterns of $LiFe_{1-x}Co_xBO_3$ (x = 0, 0.25, 0.5, 0.75, 1.00) and an enlargement zone. The impurities are indicated by asterisk(*).

Figure 4.12 ^{7}Li MAS NMR spectra of $LiFe_{1-x}Co_xBO_3$ at sample spinning rate of 30 kHz. The isotropic peaks are indicated by asterisk(*).

1. Introduction of lithium-ion battery

Renewable energy sources such as solar energy, wind, and hydroelectric power are progressively being developed as essential energy alternatives. With the growing importance of the use of renewable energy systems and EVs, HEVs, energy storage systems, it is important to ensure safety and reliable operation. The batteries are an electrochemical storage device that stores energy in the form of a difference in chemical potential and can be used anytime, anywhere when needed. Compared to primary cells, secondary batteries are more rentable, and the core of future new growth power industry because it can charge and discharge numerous times. These energy storage devices can repeatedly go through 500 charge and discharge cycles, and reversibly convert electrical energy into chemical energy. The most common rechargeable batteries are lead-acid, Ni-Cd, Ni-MH, and Li-ion.[1] Among the rechargeable batteries, lithium-ion battery (LIB) has received tremendous attention due to the largest weight capacity and the lowest redox potential. Moreover, Ragone plot in Fig. 1. shows that it has high energy and power density compared to other battery systems. However, the disadvantages of LIBs are their high cost and short life-time. The industry is expanding rapidly to develop LIBs with better efficiency.

LIB generally consists of four main components: cathode, anode, electrolyte, and separator. Although every single component of LIB is essential, the performance of LIB is highly dependent on the cathode material. The first commercial LIB was based on $LiCoO_2$ cathode material, released by Sony in the early 1990s.[2] Since then, various oxidizing and poly-anionic cathode compounds have been discovered.

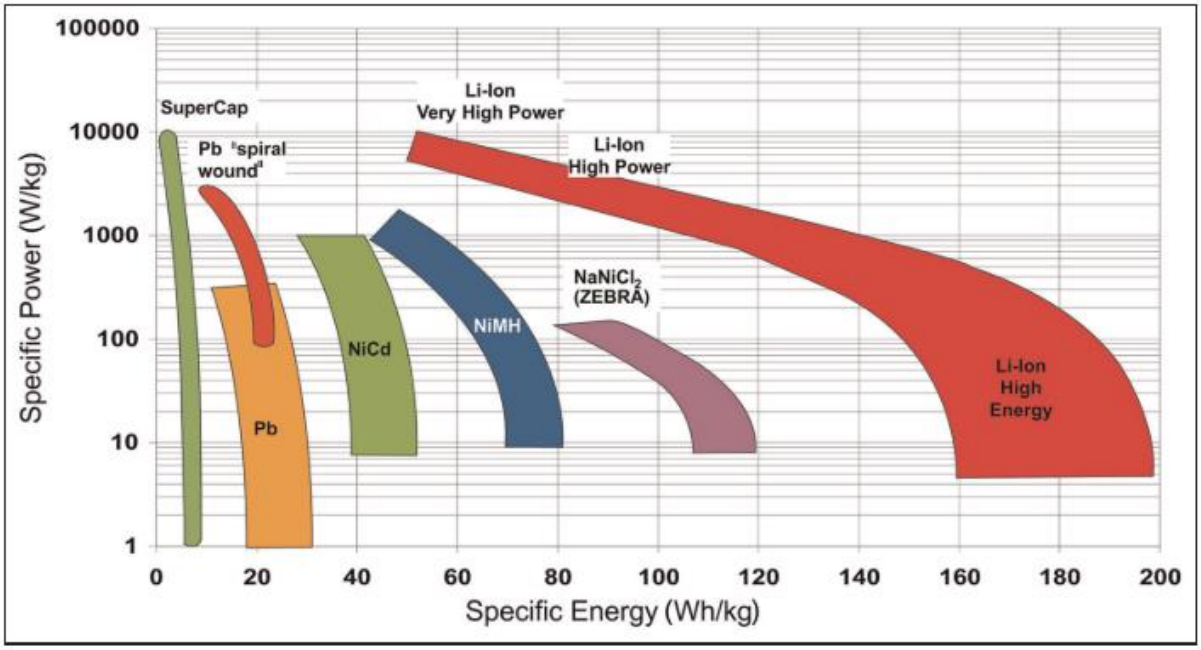

Figure 1.1 Ragone plot of various battery technologies with specification at the cell level for automotive applications.[1]

1.1 Principle of lithium-ion battery

LIB is composed of a pair of electrodes: the anode which is the source of the lithium-ion and a cathode is the acceptor of the lithium-ion. The Electrolytes provide a pathway for Li-ions as well as the separation of ion transport and electron transport.[3] It is usually an organic solvent, and the most commercially used is $LiPF_6$ in an organic solvent (e.g., the mixture of ethylene carbonate, dimethyl carbonate, and ethylmethyl carbonate). The energy storage mechanism of a lithium-ion battery is very simple. The Figure 1.2, illustrates the schematic diagram of the charge-discharge process of lithium-ion batteries. During the charging process, the Li-ion deintercalates from the lithium metal oxide (e.g. $LiCoO_2$) and passes through the Li-ion conductive electrolyte, and intercalates to the layered graphite. Lithium-ion and electron generation occurs through the following reactions:

Cathode: $Li_{1-x}CoO_2 + xLi^+ + xe^- \rightarrow LiCoO_2$

Anode: $Li_xC_6 \rightarrow xLi^+ + xe^- + C_6$

Full Cell Reaction:

$$LiC_6 + CoO_2 \rightarrow C_6 + LiCoO_2 \qquad E = 3.7\ V \text{ at } 25\ ^\circ C$$

The selection of electrodes depends on the electrochemical potential value and their electrolyte location on the HOMO-LUMO energy gap. In the expression of the electrochemical potential, μ_A and μ_C is respectively referred to as an anode and cathode. To obtain a stable cell, the LUMO of the electrolyte should be higher than μ_A, otherwise the

electrolyte will be reduced. On the other hand, HOMO of the electrolyte should be lower than the μ_C to inhibit oxidation of the electrolyte as shown in Figure 1.3.

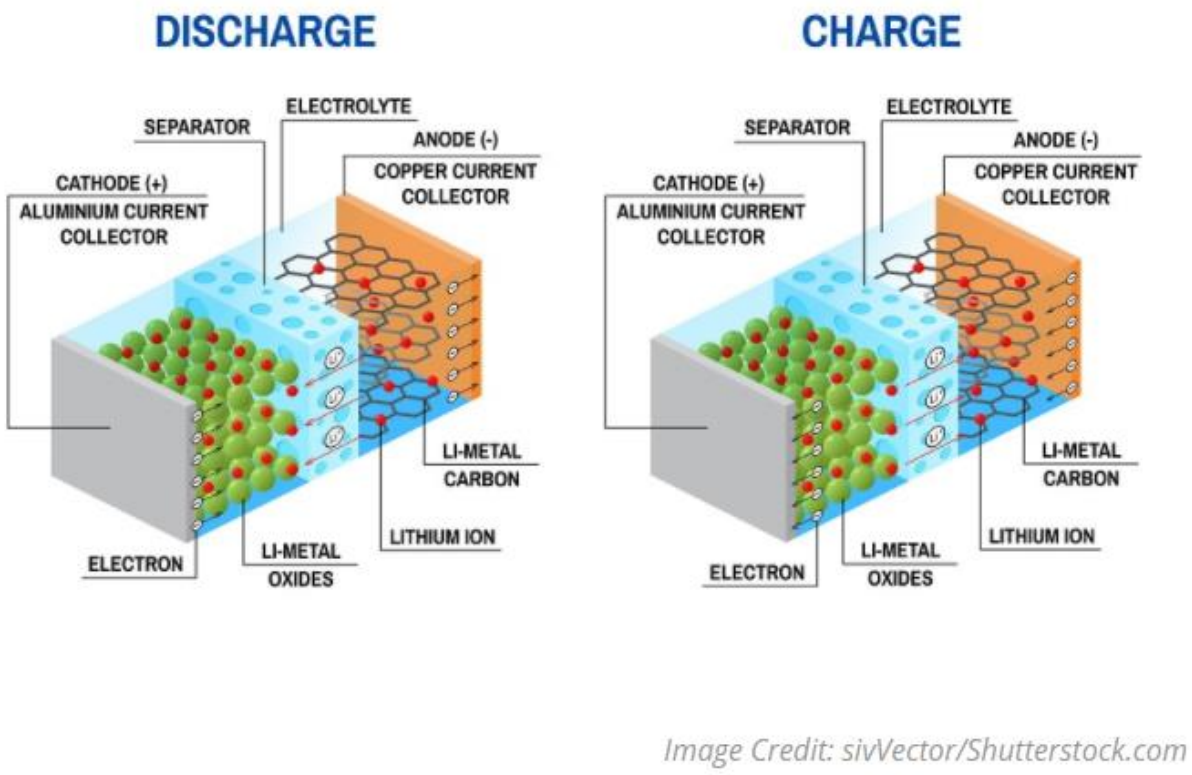

Figure 1.2 Charge and discharge mechanism of a lithium-ion battery.[4]

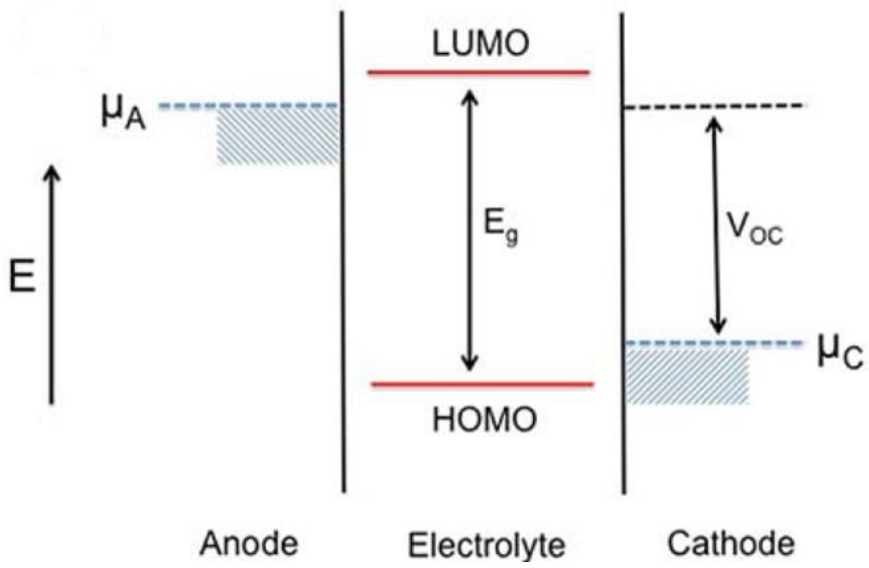

Figure 1.3 The energy diagram of electrode potential and electrolyte energy gap in the lithium-ion battery.[5]

1.2 Cathode materials

The cathode is an important part of the life cycle capability, stability, reactivity, and energy density of LIB. Typically, the cathode of LIB is composed of active material and metal foil current collector. The current collector acts as mechanical support that can exist as the electrodes of the battery and acts as a conductor that can connect the electrical energy generated by the chemicals of the two electrodes to the circuit. The most commonly used cathode current collector is the aluminum metal foil. It is resistant to corrosion due to its high oxidation state.

The electrochemical performance of LIB is related to the structural characteristics of the cathode material. The structure of the cathode material is divided into three types. The typical cathode materials for lithium-ion batteries are :

1) Layered lithium transition metal oxide $LiMO_2$ (M = Fe, Mn, Co, Ni, Ti, V, etc.). Lithium cobalt oxide having a layered structure has shown excellent success in powering small electronic devices, But the disadvantage of such material is that only half of the theoretical specific capacity can be utilized. This is because the CoO_2 layer of the $LiCoO_2$ crystal structure is separated by Li^+ ions. When more than 50% of these ions (practical capacity: 137 mAh g^{-1}) are extracted, the structure collapses and irreversibly transforms Into an electrochemically inactive phase other than electrochemically active.

2) Spinel lithium transition metal oxide. Mn-based spinels such as $LiMn_2O_4$ are attracting a lot of attention because they are rich in raw materials and are inexpensive. The octahedral MnO_6 shares the edges and forms a continuous 3D cubic array to provide the robustness and stability of the Mn_2O_4 spinel structure. Due to isotropic multidirectional Li-ion diffusion, spinel structures with cubic symmetry can reach the highest Li-ion

conductivity among intercalation materials. Moreover, the spinel cathode offers a high discharge stability good cycling, and excellent speed performance, but a capacity of less than 150 mAh g^{-1} is achieved while cycling above 3V.[6]

3) Poly-anion compounds (e.g., phosphate, silicate, fluorine phosphate, fluorine silicate, borate)[7]. Polyanionic compounds are a kind of material in which tetrahedral polyanionic structural units $(XO_4)^{n-}$ (X = P, S, As, Mo, or W) with strong covalent bonds are coordinated with the MOx (M = transition metal) polyhedron.[8] These polyanions occupy the lattice position and simultaneously increase the cathodic redox potential to stabilize the structure. Therefore, the polyanion cathode materials not only ensure the fast conduction of alkali ions in the framework structure but also improves the structural stability during the metal redox process. The polyanion cathode material not only ensures the fast conduction of alkali ions in the framework structure, but also improves the structural stability during the metal redox process. Additionally, properties such as cycle stability, safety, environmental friendliness, and potentially low cost make them the most competent electrode materials.

The schematic framework of the crystal structure for the battery insert material is depicted in Figure 1.4.

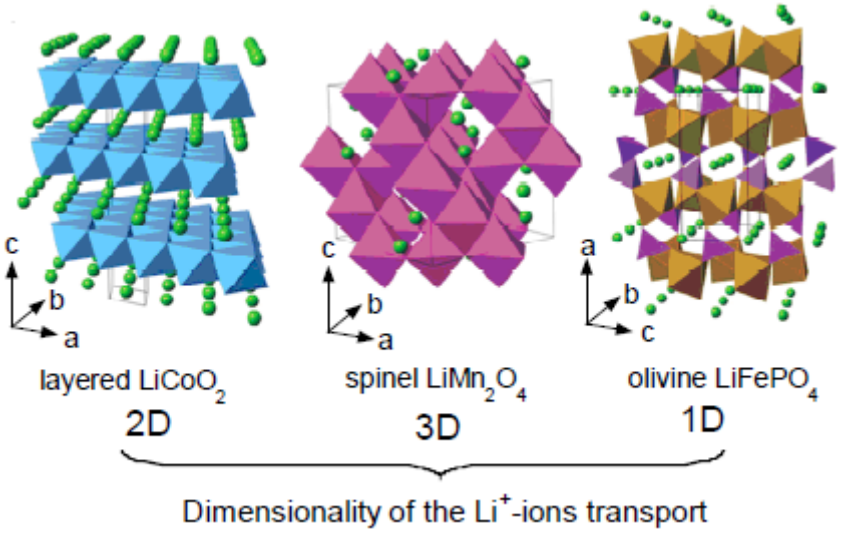

Figure 1.4 Crystal structure of the three lithium-insertion compounds. The green balls represent Li^+.[9]

1.3 Borate based cathode materials

The various combinations between poly-anions and transition metals allow tuning the electrochemical properties of these materials.[10] Legagneur et al. first reported the electrochemical properties of $LiMBO_3$ (M = Mn, Fe, and Co) as cathodes of a Li rechargeable battery.[11] Borate-based cathode materials possess several attractive properties, such as high theoretical capacity (222 mAh g^{-1}), high energy density (660–860 Wh/kg), lightweight, small volume change during cycling (c.a. 2%[10]), high stability against oxygen loss, abundance, and environmentally friendly material.[12] However, like other polyanion cathodes, they has low electrical conductivity, which limits their practical application.[13, 14] LMB (M = Mn, Fe, Co) compounds crystallize in the monoclinic space group C2/c.[11, 15, 16] The structure is composed of edge-sharing MO_5 trigonal bipyramids which are bound together via BO_3 planar triangles to form a polyanionic framework.[14] The monoclinic crystal structure of LM B (M = Mn, Fe, Co) is shown in Figure 1.5. Transition metal (TM) ions occupy the trigonal bipyramidal sites and are shifted slightly from the center of this region, so it makes two different crystallographic regions for the M1 and M2 regions. But The distances between the M1 and M2 sites are so small, which is about 0.3 Å.[10] Li-ions are surrounded by four oxygen ions and occupy two different sites (Li1 and Li2 sites) whose occupancies are 0.5 for both sites (Figure 1.6). Table 1 shows the calculated lattice parameters of Li_xMBO_3 ($0<x<1$, M = Mn, Fe, Co). The lithiated phase lattice parameters are consistent within 2% of the reported experimental values.[11, 15, 16] Experimental results for the fully delithiated state have not yet been reported, but Table 1 predicts these lattice parameters.[10] The TM ions of $LiMBO_3$ (M = Mn, Fe, Co) occupy trigonal bipyramidal sites surrounded by five oxygen ions, the 3d bands of TM ions are split into the e'', e', and a' bands by crystal-field theory. (Table 2) The MO_5 trigonal bipyramid of the schematic energy

splitting is shown in Figure. 1.7. and the electron occupation of $LiMBO_3$ (M = Mn, Fe, Co) appears in Figure 1.8. In addition, it has been shown that polyanions enable low transition metal redox energies through inductive effects, and allow some sort of adjustment of such energies. Many recent studies tend to provide a preliminary assessment of the inducing effects of the much lighter BO_3 group. This makes borate an attractive new cathode material for lithium-ion batteries.[16]

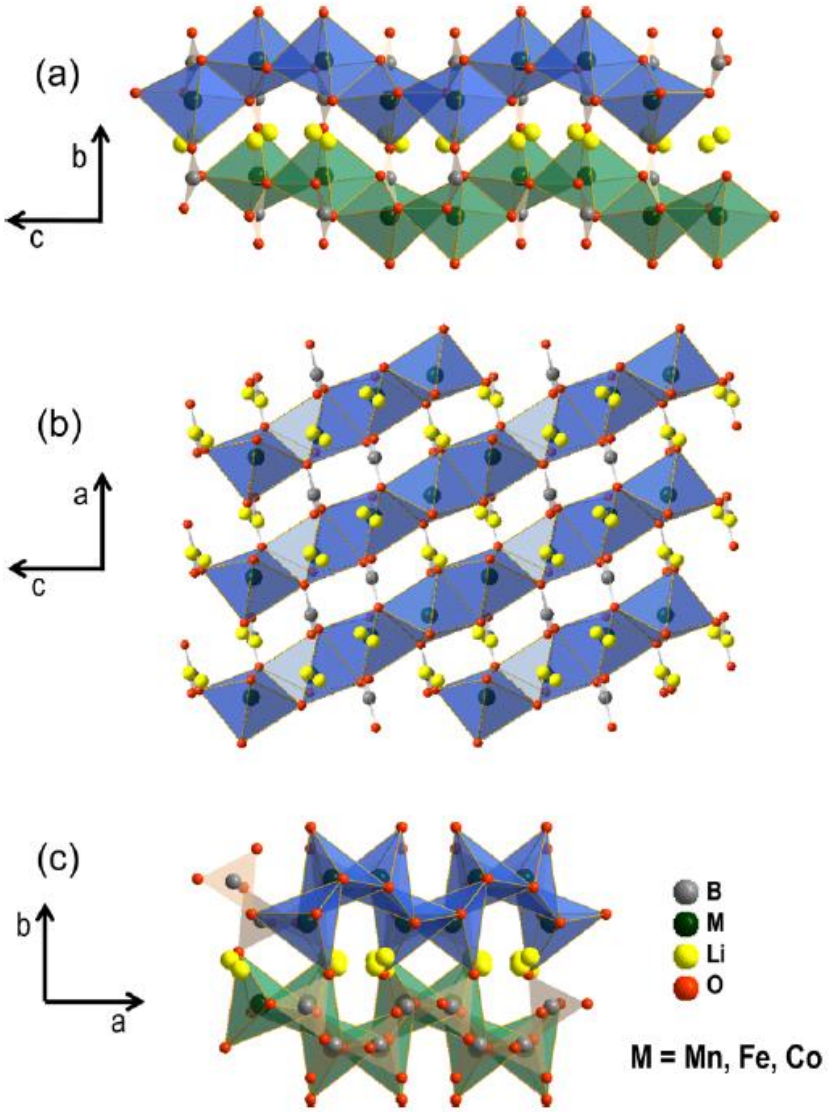

Figure 1.5 Monoclinic $LiMBO_3$ (M = Mn, Fe, Co) crystal structure along the (a) a-axis, (b) b-axis, and (c) c-axis.[14]

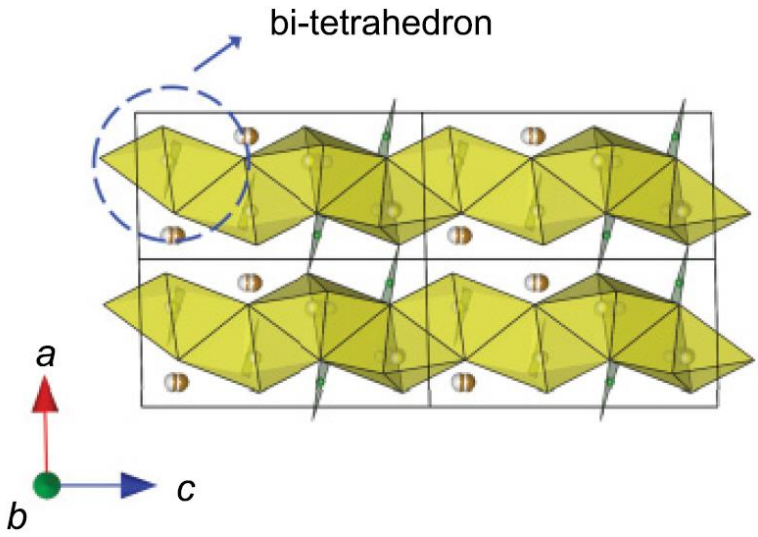

Figure 1.6 Edge-shared chains of LiO_4 parallel to the [001] direction.[10]

Table 1. Calculated and experimental lattice parameters of $LiMBO_3$ (M = Mn, Fe, and Co). ΔV indicates volume change at delithiated $LiMBO_3$.[10]

	a (Å)	b (Å)	c (Å)	β (deg.)	ΔV
$LiMnBO_3$	5.225	9.013	10.446	91.82	2.0%
$MnBO_3$	5.249	8.971	10.135	91.11	
exp-$LiMnBO_3$ (Ref. 40)	5.19	8.95	10.37	91.80	
$LiFeBO_3$	5.230	9.024	10.236	91.36	1.4%
$FeBO_3$	5.241	8.957	10.150	90.92	
exp-$LiFeBO_3$ (Ref. 18)	5.16	8.92	10.19	91.36	
$LiCoBO_3$	5.164	8.898	10.189	91.41	1.6%
$CoBO_3$	5.199	8.852	10.005	90.24	
exp-$LiCoBO_3$ (Ref. 39)	5.13	8.84	10.10	91.36	

Table 2. Electronic structures of Li_xMBO_3 (x = 1 and 0, M = Mn, Fe, and Co).[10]

	Electron configuration	Net moment (1/2 μB)	Bandgap (eV)
$LiMnBO_3$	$e''^{2}\ e'^{2}\ a'^{1}$	4.77	3.15
$MnBO_3$	$e''^{2}\ e'^{2}\ a'^{0}$	3.98	0.49
$LiFeBO_3$	$e''^{3}\ e'^{2}\ a'^{1}$	3.79	3.19
$FeBO_3$	$e''^{2}\ e'^{2}\ a'^{1}$	4.32	1.59
$LiCoBO_3$	$e''^{4}\ e'^{2}\ a'^{1}$	2.85	3.26
$CoBO_3$	$e''^{3}\ e'^{2}\ a'^{1}$	3.23	0.76

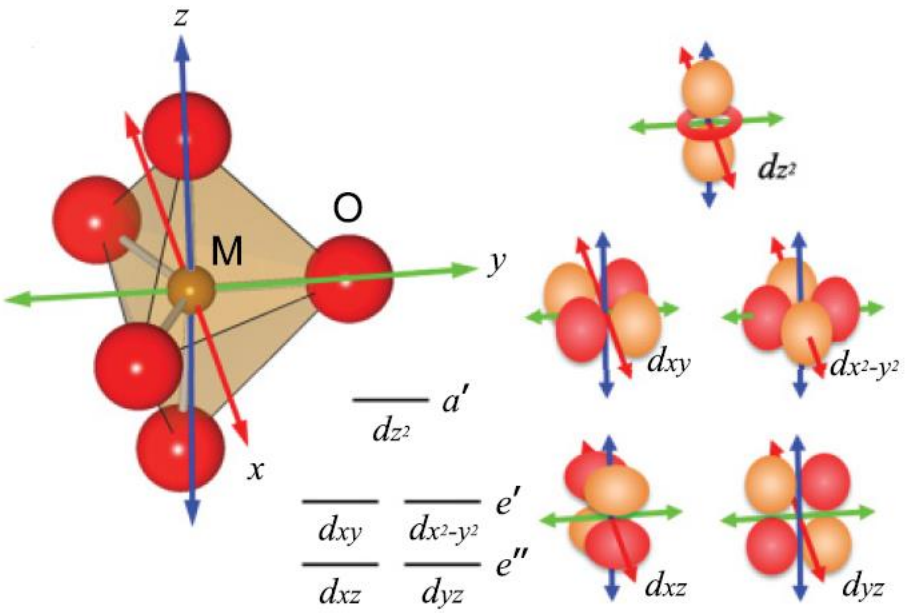

Figure 1.7 MO_5 trigonal bipyramid and schematic energy levels of the 3d bands of the TM ion.[10]

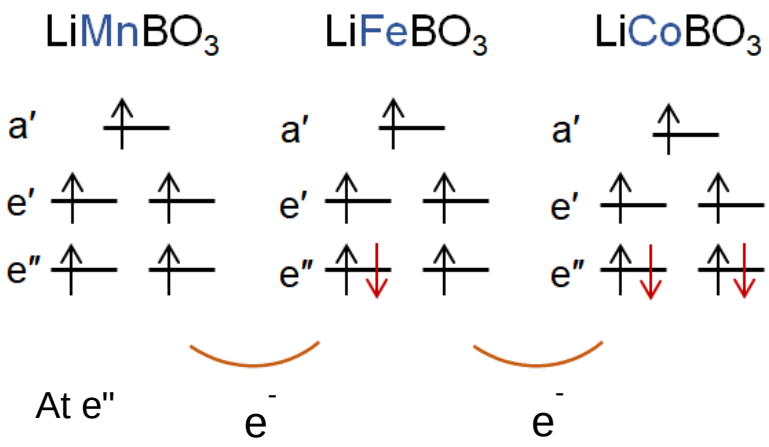

Figure 1.8 Scheme of energy levels and occupied electrons of $LiMBO_3$.

1.3.1 Lithium iron borate ($LiFeBO_3$)

The $LiFeBO_3$ (LFB) compound was first synthesized by Legagneurn et al.[11] by solid-state synthesis. A large theoretical capacity of 220 mAh g^{-1} is calculated based on the LFB chemical formula, which is much larger than the 170 mAh g^{-1} for $LiFePO_4$. Furthermore, the density of LFB is 3.46 g/cm^3, which is close to that of $LiFePO_4$. And it is suitable to maximize the volume energy density, due to the minimum volume occupation of planar triangle BO_3 oxyanion unit.[15] Also it exhibits a larger reversible capacity (ca. 200mAh g^{-1}) under moderate current density with surprisingly small volume change (ca. 2%).[15]

The electrochemical performance of LFB was first investigated in 2001 when it was reported at a very low rate (C/250) with a capacity of less than 10 mAh g^{-1}.[11] When Dong et al. looked at the material again, he used a carbon coating to facilitate electron transport during cycling.[16] Despite being able to achieve better electrochemical performance in terms of the observed capacity (150 mAh g^{-1}), a large polarization was observed and only 60 mAh g^{-1} was delivered below 4.5V when charging.[17] Recently, Yamada et al. carefully prepared electrode samples in an inert Ar atmosphere to achieve a large reversible capacity of about 190 mAh g^{-1}.[15] The underlying mechanisms of performance degradation and capacity loss are still unclear, and ways to improve the performance of this promising material at high speeds are still in demand. Understanding the performance degradation issue will be an important step towards minimizing performance degradation and improving battery performance. LFB and its alternative variants could be good cathode candidates for next-generation lithium-ion batteries if these performance improvements are realized.[17]

1.3.2 Lithium manganese borate ($LiMnBO_3$)

$LiMnBO_3$ (LMB) having a monoclinic phase (referred to as m-$LiMnBO_3$) at low temperature (T<650 ℃) and a hexagonal phase (referred to as h-$LiMnBO_3$) at high temperature (T~800 ℃).[14]

Among them m-$LiMnBO_3$ is a system of particular interest due to its large one-electron theoretical capacity of 222 mAh g^{-1}.[10, 18] However, in many studies, monoclinic m-$LiMnBO_3$ displays limited cycling performance with noticeable capacity fading compared to other cathode materials.[18, 19] Most importantly, an in-depth explanation of the major reasons for the lifetime limitation of m-$LiMnBO_3$ is still lacking.[18, 19] The structural stability of cathode material, especially the stability of delithiated states, is important to understand the cycling behavior.[20] Although electrochemical charging and chemical delithiation of m-$LiMnBO_3$ has been attempted in previous studies, the fully delithiated state could not be reached electrochemically, and amorphization occurred in preference to full oxidation.[21] But with respect to the general trend of voltage generation by the M^{3+}/M^{2+} redox couple in various solids, Mn has a higher voltage than Fe. (i.e., Ni > Co > Mn >Fe of which the voltages are expected to be 4.8, 4.4, 3.7,and 3 V, respectively).[18]

1.3.3 Lithium cobalt borate ($LiCoBO_3$)

There are few reports of lithium cobalt borate ($LiCoBO_3$, LCB). The cobalt system has a higher voltage compared to LMB and LFB.[22] The average redox potential of Co^{2+}/Co^{3+} is ca. 4 V vs. Li/Li^+ in LCB. With an excellent combination of high theoretical capacity (ca. 215 mAh g^{-1}) and expected 4V operation, LCB can provide a higher energy density than Li_xCoO_2 ($0.5 \leq x \leq 1$). In addition, the easy to handle and safe properties make LCB an ideal cathode.[23]

Yamashita et al. improved the reversible capacity of LCB from C/20 to 30mAh g^{-1} and showed that the electrochemical activity is concentrated at 4V in this compound.[23] However, reaching the theoretical capacity of this compound seems difficult due to the limitations induced by the structural/chemical instability of fully delithiated LCB.

2. Introduction of Nuclear Magnetic Resonance (NMR)

2.1 Principle of NMR

Nuclear magnetic resonance (NMR) spectroscopy is basically a type of absorption spectroscopy. The NMR measurement is absorbing radiofrequency (RF) radiation energy specific to the nucleus is placed in a strong magnetic field. Upon absorption under certain conditions, the nuclei begin to resonate and different atoms within a molecule resonate at different frequencies. RF waves are low-energy electromagnetic radiation with frequencies from several kHz to several hundred GHz. The energy of RF wave radiation is insufficient to cause vibrations, rotations, or electron excitation of atom or molecules but it is enough to affect atomic nuclear spins, which allow a detailed analysis of the molecular structure.[24]

The Nucleus has spin angular momentum that is quantized in size and direction. To perform NMR analysis, the nuclear spin quantum number (I) should not be zero and have a magnetic moment (μ). Nuclei containing even numbers of both protons and neutrons have I=0 and therefore cannot undergo NMR. (^{12}C, ^{16}O etc.) But, every element in the periodic table has at least one isotope that can experience NMR that is NMR active when placed in a magnetic field. The different nuclear spin quantum number for the nuclide is shown in Figure 2.1.

The nuclear spins are under the influence of the external magnetic field, are aligned causing a net magnetic moment to build up along the B0 direction as shown in Figure 2.2. (which is commonly defined to be the z direction). Nuclear spin states must be quantized to observe the resonance phenomenon of nuclear spins. The number of spin states has 2I+1 and when active spins are placed in a strong magnetic field, it aligns them according to their energy state, which is called the Zeeman Effect. The arrangement of nuclear spins can be

aligned in the same or opposite direction as the magnetic field. These two nuclear spin alignments have different energies, and these energy differences are related to the Larmor frequency. In the case of ^{1}H nucleus, it has two energy states since its nuclear spin quantum number is 1/2 (I = 1/2). Figure 2.3 illustrates that Zeeman Effect.[25, 26]

Absorption of the radiation causes the nuclear spin to realign or flip in the higher-energy direction. After absorbing energy, the nuclei will re-emit RF radiation and return to the lower-energy state. This process involves the thermal equilibrium of longitudinal magnetization which is manipulated by RF pulses. The RF pulses are applied to the sample through an RF coil used for both manipulation of the spin system and signal detection.

Because of internal NMR interactions and so-called spin-spin relaxation processes (T2 relaxation), a relatively quick loss of this coherency occurs as well as a slow recovery to the longitudinal magnetization. This causes a decay of the induced voltage, which is measured as the free induction decay (FID). FID signals are transformed by Fourier transformation (FT), in which the voltage-time signal is translated into an intensity-frequency signal (Figure 2.4).[27]

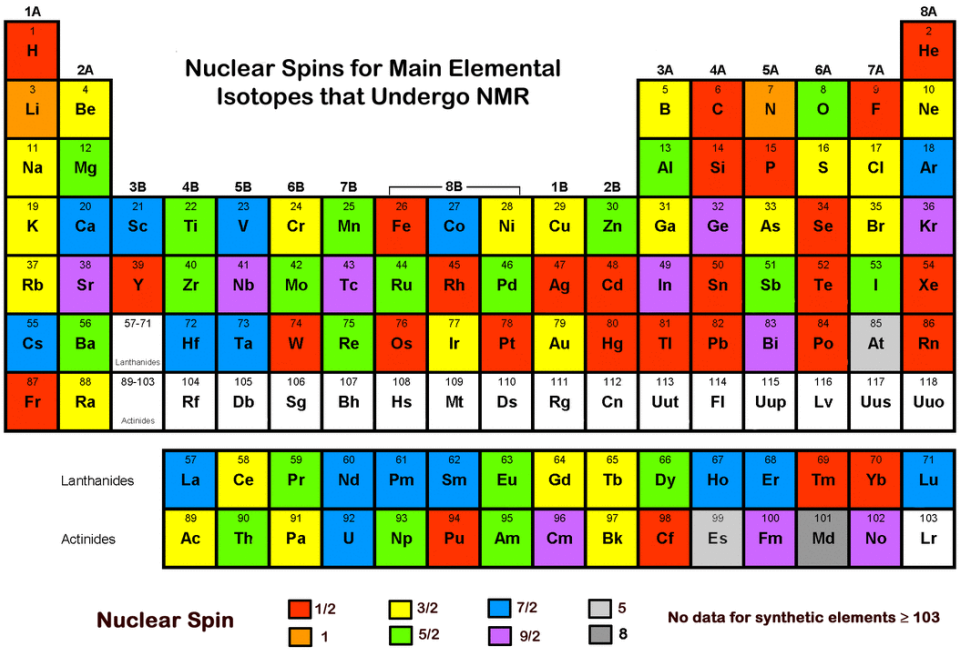

Figure 2.1 Distribution of nuclear spin (I) values for the major NMR active isotopes in the periodic table.[28]

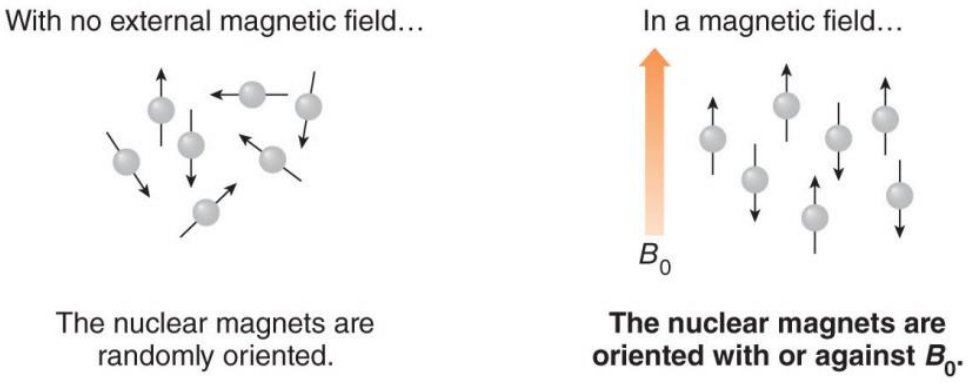

Figure 2.2 The orientation of the nuclear magnet according to the presence of a magnetic field.

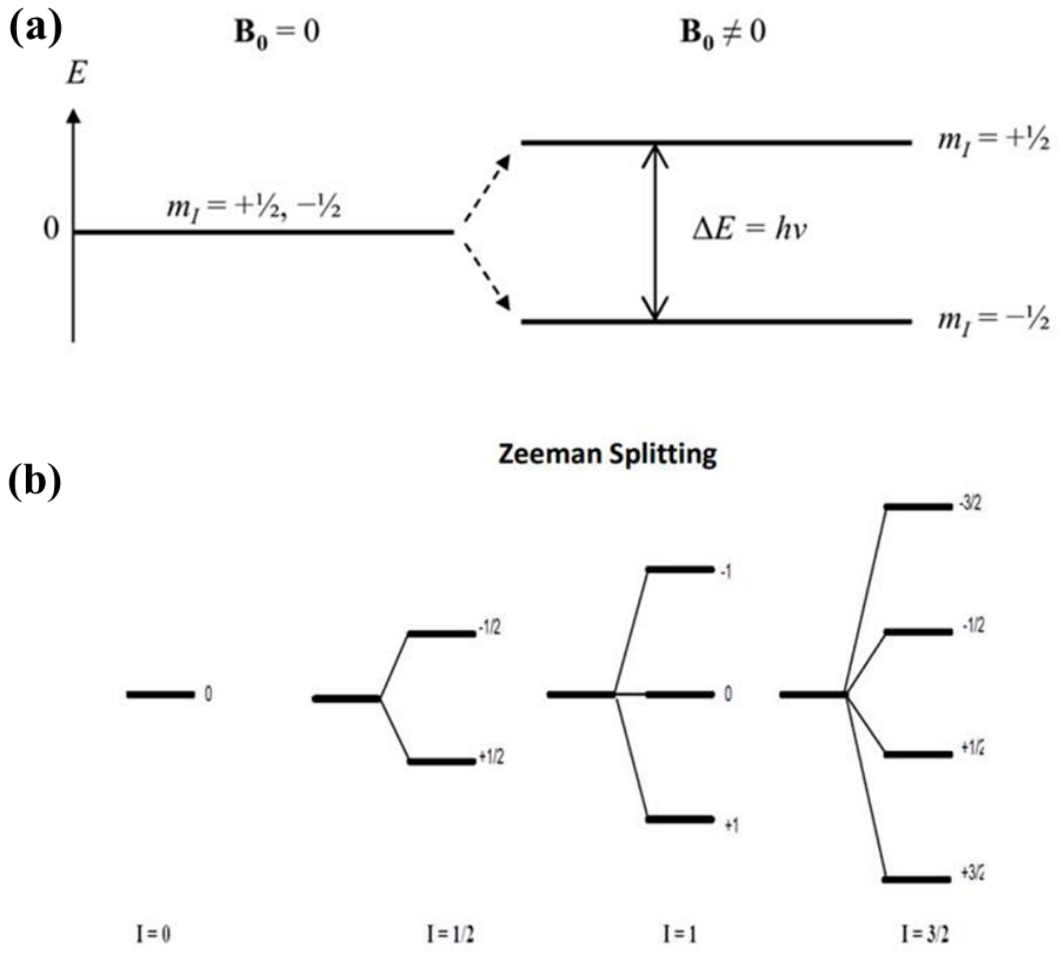

Figure 2.3 Zeeman Splitting of (a) a spin-½ nucleus under the magnetic field B_0

(b) Energy levels (I > 0)[26]

2.1.1 Boltzmann distribution

The number of nuclei in each spin state can be described by the Boltzmann distribution equation demonstrated in Equation 2.1. When there is no external magnetic field, the nuclear spins are randomly oriented in any direction, but when a magnetic field (B_0) is applied, the nuclear spins are oriented in the same direction or in opposite directions. Therefore, energy becomes different. Spins in the same direction as the magnetic field (B_0) are more stable and exist in a lower energy state (α) and spins in the opposite direction are in a higher energy state (β).

$$\frac{N_\alpha}{N_\beta} = e^{-\Delta E/kT} \tag{2.1}$$

$$\Delta E = h\nu = \frac{\gamma h}{2\pi} B_0 \tag{2.2}$$

Substituting Equation 2.2 into Equation 2.1 gives

$$\frac{N_\alpha}{N_\beta} = e^{-\left(\frac{\gamma h B_0}{2\pi kT}\right)} \tag{2.3}$$

(N_α : number of spins in the higher energy state, N_β : number of spins in the lower energy state, k : Boltzmann's constant (1.3804×10^{-23} J K^{-1}), T : absolute temperature, h : plank's constant (6.626×10^{-34} J·s))

Spins of the nucleus with a low energy state can be excited to a higher energy state by irradiating the nucleus with electromagnetic radiation of the correct energy. The absorption of energy occurs during this transition.[29]

2.1.2 T_1 (Spin-lattice relaxation) and T_2 (Spin-spin relaxation)

In NMR, a magnetic field generated by flowing an alternating current to a coil is called the B_1 magnetic field. When a pulse B_1 magnetic field is generated, the spin of the nucleus is aligned in the same or opposite direction to the external magnetic field along the z-axis. At this moment, the nucleus spin of the z-axis can be inverted to the x-y plane by injecting a short pulse. After the pulse injection, the spin system tries to return to the equilibrium state, and the time taken for this is called the relaxation time. The relaxation time is divided into T_1 (Spin-lattice relaxation time) and T_2 (Spin-spin relaxation time) which indicates how fast the nucleus spins are magnetized in the z-axis. At the equilibrium state, the net magnetization vector lies in the same direction as the external magnetic field (B_0) which is called equilibrium magnetization (M_0).

When energy is applied to the system, the spin system is saturated and M_z becomes zero. In this saturation state, the time that it takes for M_z to return to its original equilibrium state is called T_1 (spin-lattice relaxation time) as shown in Figure 2.4.

When the net magnetization lies in the x-y plane by a pulse, it rotates about the z-axis at the Larmor frequency and it is called precession. Precession and net magnetization experience slightly different magnetic fields in each spin, and eventually rotate at different Larmor frequencies resulting in de-phasing. As a result, a larger de-phasing occurs over time. The time required for the transverse magnetization M_{xy} to return to the equilibrium state is referred to as T_2 (spin-spin relaxation time) and is represented by the following illustrated in Figure 2.5.

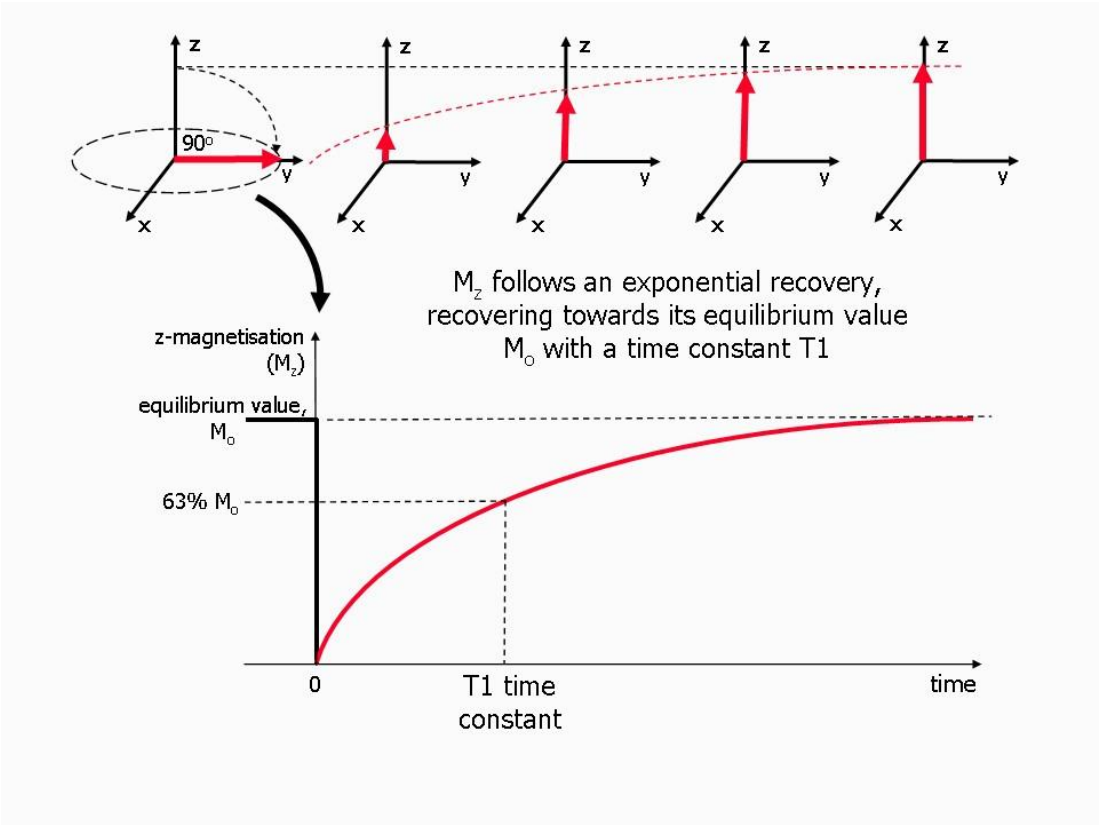

Figure 2.4 T_1 relaxation process.[30]

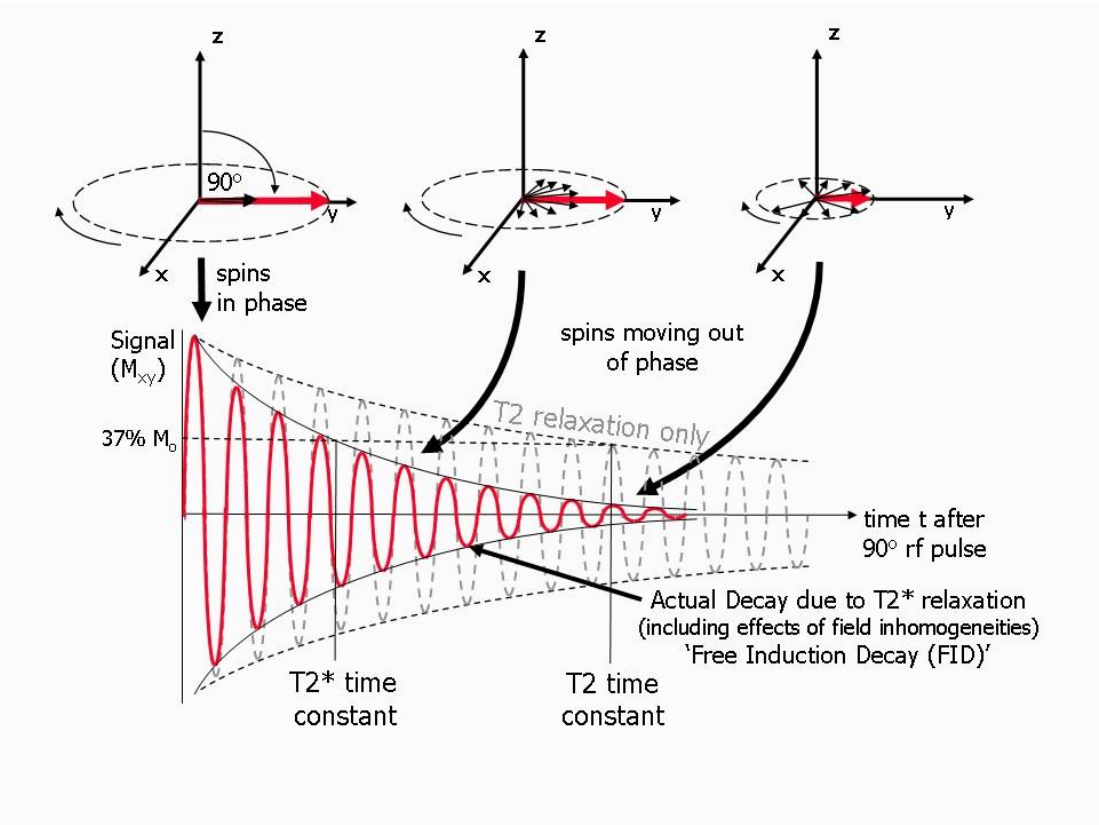

Figure 2.5 Transverse (T_2 and T_2*) relaxation processes.[30]

2.2 Solid-state NMR

In comparison to solution NMR which is used for the analysis of liquid samples, the solid-state NMR is performed on solid samples. Solid-state NMR instruments can measure samples in virtually any state, not just common solids. And in solution NMR, spectra consist of a series of very sharp transitions, due to averaging of anisotropic NMR interactions by rapid random tumbling. By contrast, solid-state NMR spectra are very broad, as the full effects of chemical shift anisotropic, dipole-diploe coupling, and orientation-dependent interactions are observed in the spectrum. The effect of broadening according to sample type is demonstrated in Figure 2.6. High-resolution NMR spectra can provide the same type of information that is available from corresponding solution NMR spectra. But we need a number of special techniques/equipment, including magic-angle spinning, cross-polarization, special 2D experiments, enhanced probe electronics, etc.[31]

In particular, for single crystal samples, changes in the resonant frequency are observed and analyzed according to the relative direction to the magnetic field. In addition, the presence of broad NMR lineshapes, once thought to be a hindrance, actually provides much information on chemistry, structure, and dynamics in the solid-state.[31] .

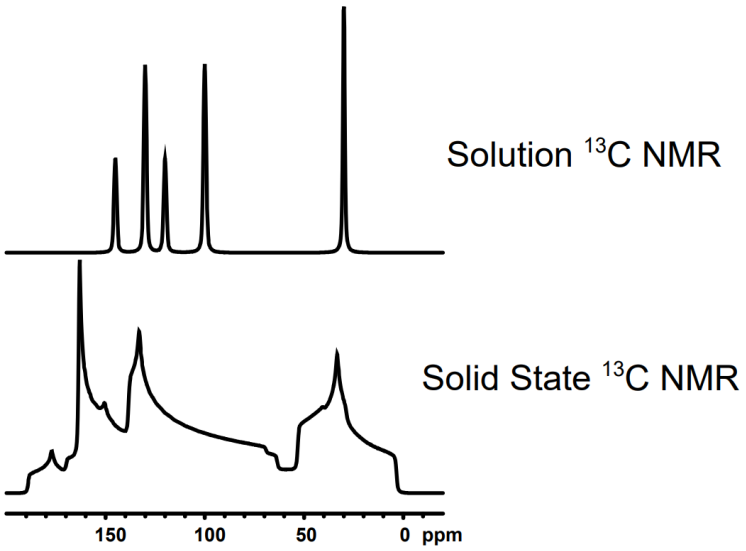

Figure 2.6 Comparison of ^{13}C NMR spectra in solution and solid-state.[31]

2.2.1 Magic Angle Spinning (MAS) technique

MAS NMR is a technique for obtaining high-resolution NMR data from solids. Contrary to solution NMR, where anisotropic interactions are averaged by the rapid tumbling of molecules, in solid-state NMR, interactions such as the chemical shift anisotropy (CAS) and dipolar coupling dominate. As a consequence, the spectral line width of nuclei in solids is rather broad.[32] In order to overcome this problem in the solid-state, the MAS technique, known since the 1950s, is usually employed.

1) The chemical shift anisotropy because of the anisotropy of the electronic environment that varies depending on the direction, which is caused by the surrounding electrons that modify the local environment of the nucleus. Its equation is demonstrated in Equation 2.4.

$$\Delta\omega = \omega_0\delta(\frac{3}{2}+\eta)(3cos^2\theta - 1) \quad (2.4)$$

2) The dipolar coupling (interaction) that occurs by direct spatial coupling between nuclei. The equation is demonstrated in Equation 2.5.

$$\Omega_{ji} = \frac{\alpha\gamma_{i\gamma_j}}{3\sqrt{2}r_{ij}^3}(1 - 3cos^2\theta_{ij}) \quad (2.5)$$

3) The quadrupole interaction caused by the interaction between the electric quadrupole moment of the nuclei and the asymmetric electric field gradients surrounding the

nucleus and this type of interaction occurs when the nuclear spin I is greater than ½. The equation is expressed in Equation 2.6.

$$H_Q = \frac{e^2qQ}{4I(2I-1)}\left(\frac{3cos^2\theta-1}{2}\right)[3m^2 - I(I-1)] \quad (2.6)$$

These three interactions include in the term of $3cos^2\theta - 1$ and when the terms to be 0, sharp peaks appear. The sample must be spin around an axis that is oriented at an angle 54.74° to the magnetic field B_0.

$$(3cos^2\theta - 1) = 0,\ \theta = 54.74° \quad (2.7)$$

This technique is called Magic Angle Spinning (MAS). Schematic representations of the MAS experimental effect are shown in Figure 2.7 and Figure 2.8

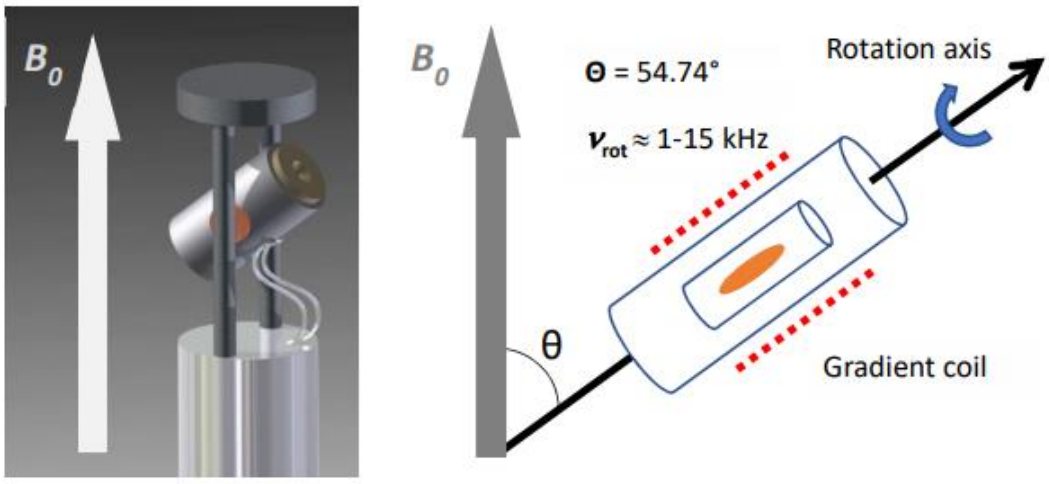

Figure 2.7 Representation of a MAS NMR probe head with an orientation of the stator at an angle (θ) of 54.7◦ between the axis of rotation and B_0.[33]

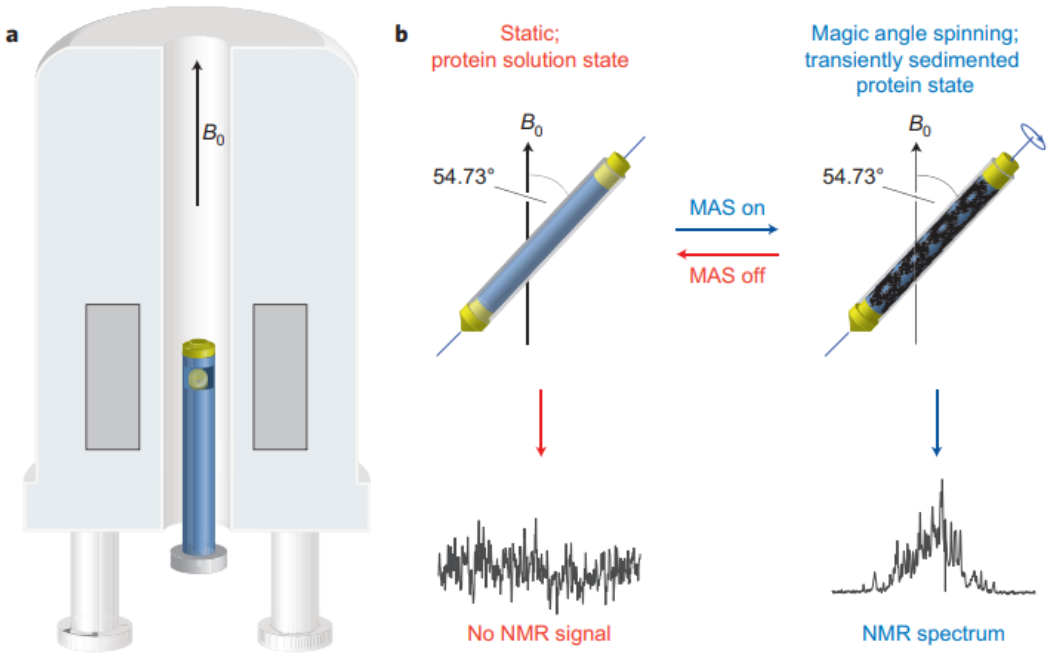

Figure 2.8 A schematic representation of a transient sedimentation NMR experiment. (a) An NMR magnet with a MAS probe. (b) Top: In a MAS probe, the NMR sample rotor is inclined at the 'magic angle' axis (54.73^{o} with respect to the static magnetic field B_0).[34]

2.2.2 Spin echo pulse sequence (Hahn echo)

Apart from the FID, there are two other commonly encountered types of signal in spin-½ NMR experiments: the spin echo also known as Hahn echo (Hahn, 1950), and the stimulated echo. Commonly, Spin echo is generated by applying a 180° refocusing RF pulse after a 90° excitation pulse. Thereby, the 90° pulse is called excitation pulse and the 180° pulse is refocusing pulse (Figure 2.9). Spin echo, as opposed to FIDs, can be produced using two RF pulses in succession.[26] Echo can be used to overcome dead time limitations, which are often encountered in observation of resonances from solid-state materials (as illustrated in Figure 2.10).

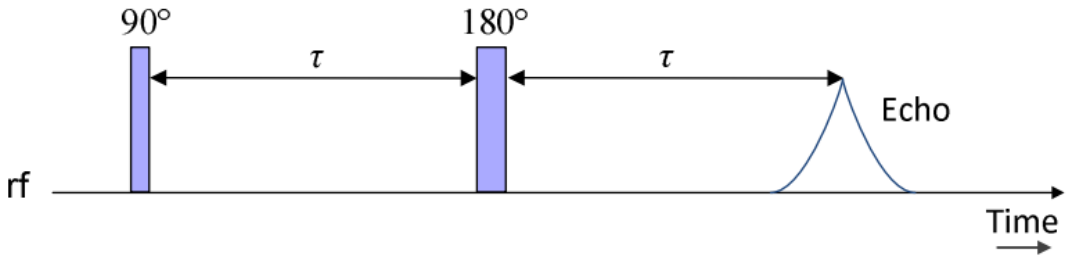

Figure 2.9 Basic NMR pulse sequences: Hahn echo[26]

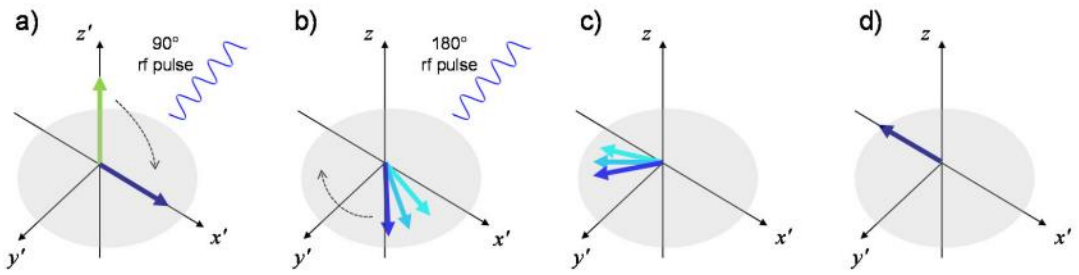

Figure 2.10 The spin-echo: (a) Application of a 90° rf pulse at t = 0 tips the magnetization vector from its equilibrium state (green) into the x-y plane (dark blue); (b) In the x-y plane, spins at different locations lose phase coherence due to field inhomogeneity and begin to process at different frequencies, with faster spins shown in darker blue and slower spins in lighter blue. Application of a 180° rf pulse at t=τ rotates the magnetization about the y-axis; (c) The order of the spins is now reversed, with the slower spins 'ahead' of the faster spins; (d) this leads to the spins regaining coherence or 'refocusing' at a point in time t=2τ.[26]

3. Experimental

3.1 Synthesis

The solid-state reaction is the most common and economic method to prepare cathode material. This method is simple and easy to industrialize. The solid precursors are planetary milled together with zirconia balls, followed by heat-treatment in a furnace. In the case of monoclinic Li*M*BO_3 (*M* = Mn, Fe, Co), the raw material involves all of lithium (e.g., LiH_2PO_4, Li_2CO_3, and LiOH), metal (e.g., $FeC_2O_4{\cdot}2H_2O$, $MnCO_3$ and $CoC_2O_4{\cdot}2H_2O$) and borate (e.g., B_2O_3 and H_3BO_3) source.

3.1.1 Synthesis of $LiFe_{1-x}Mn_xBO_3$ (x = 0, 0.25, 0.5, 0.75)

A mixture material composed of iron and manganese, $LiFe_{1-x}Mn_xBO_3$ (x = 0, 0.25, 0.5, 0.75), used as a cathode material for lithium secondary batteries were prepared by solid-state reaction. Stoichiometric amounts of Li_2CO_3 (Aldrich, ≥ 99%), $FeC_2O_4 \cdot 2H_2O$ (Junsei, ≥ 99%), $MnCO_3$ (Aldrich, ≥ 99%), and BH_3O_3 (Daejung, ≥ 99%) were without further purification. Stoichiometric amounts of the reactants in acetone media were planetary milled with zirconia balls for 4 h at 300 rpm and dried in an oven at 80 ℃ for approximately 24 h. The dried mixture was ground with a mortar and pestle. The obtained precursor powder was purged to prevent oxidation in a tube furnace under pure argon gas for 3 h and first sintered at 350 ℃ for 3 h due to organic partly decomposing and subsequently sintered at 550 ℃ for 10 h. It is heated at a rate of 5 ℃ min^{-1} and finally cooled to room temperature. This scheme process is shown in the Figure 3.1.

3.1.1 Synthesis of $LiFe_{1-x}Co_xBO_3$ (x = 0, 0.25, 0.5, 0.75)

A mixture material of iron and manganese, $LiFe_{1-x}Co_xBO_3$ (x = 0, 0.25, 0.5, 0.75), were prepared by a multiple-step process with solid-state reaction. First, orthoborate $Co_3(BO_3)_2$ was obtained with B_2O_3(Alfa Aeasar, ≥ 99%) and $CoC_2O_4 \cdot 2H_2O$ (Aldrich, ≥ 99%) were planetary milled at 300rpm for 3h and heated at 800℃ for 6h in air. It is heated at a rate of 5 ℃ min^{-1} and finally cooled to room temperature. Then, $Co_3(BO_3)_2$ were mixed with stoichiometric amounts of Li_2CO_3 (Aldrich, ≥ 99%), $FeC_2O_4 \cdot 2H_2O$ (Junsei, ≥ 99%), and BH_3O_3 (Daejung, ≥ 99%) for 3 h at 300rpm. After that material was dried in an oven at 80 ℃ for approximately 12 h. The obtained precursor powder was purged to prevent oxidation in a tube furnace under pure argon gas for 3 h and sintered at 530 ℃ for 6 h. It is heated at a rate of 5 ℃ min^{-1} and finally cooled to room temperature. This scheme process is shown in Figure 3.2.

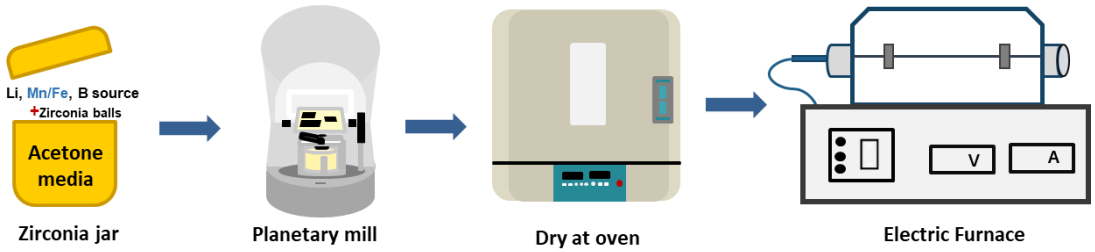

Figure 3.1 Solid-state synthetic procedures of $LiFe_{1-x}Mn_xBO_3$ as a cathode material.

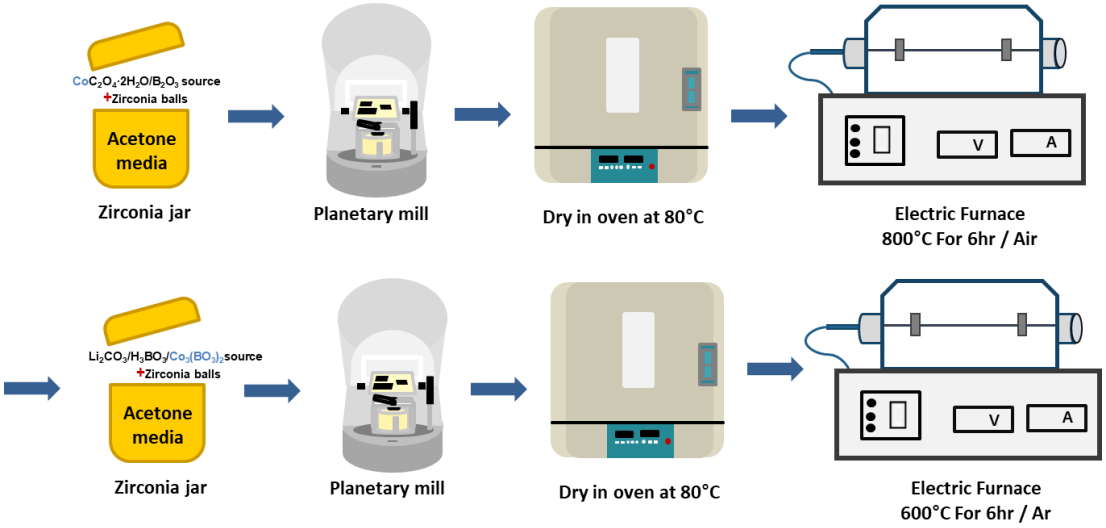

Figure 3.2 Solid-state synthetic procedures of $LiFe_{1-x}Co_xBO_3$ as a cathode material.

3.2 General characterization

The evolution of crystalline phases as a function of heating temperature was studied using X-ray diffraction (XRD, Rigaku Ultima 4, Japan) with Cu Kα radiation (λ = 1.5406 Å). The operating conditions of the XRD were 50 kV and 40 mA over the 2θ range of between 10 and 80° at a step size of 0.01° in continuous scan mode at 2° min^{-1}. ICSD provided by FIZ Karlsruhe was used to identify the phases in the samples. LIBS spectra of the samples were collected using a commercial Laser-induced breakdown spectroscopy instrumentation (LIBS, J200 Tandem LA-LIBS Instrument, Applied Spectra, Inc.) equipped with a Nd : YAG laser (maximum energy: 25 mJ) generating 266 nm radiation (a harmonic wavelength) with a pulse width of 5 ns. The instrument collected spectra with a resolution of 0.10 nm in the 185–1048 nm range using a six-channel CCD. The delay time, laser power, and illumination spot size were set to 0.4 μs, 12.5 mJ, and 100 μm, respectively, for acquisition of the LIBS spectra.

3.3 Electrochemical test

The electrochemical measurements were conducted using CR 2016 typed coin cells. The coin cells were comprised of the cathode electrode (working electrode), metallic Li foil as the anode electrode, electrolyte, and separator. To prepare the working electrode, a mixture of 80 wt.% active material (synthesized cathode material), 10 wt.% conductive material (super-P) and 10 wt.% poly(vinylidene fluoride) (PVDF, Aldrich, Mw = 534,000) was mixed in *N*-methyl-2-pyrrolidone (NMP) until viscosity slurry. The obtained slurries were pasted onto an aluminum foil substrate (thickness 15 μm) using a doctor blade and followed by drying in a vacuum oven at 80 ℃ for 2 h. After that, they were squeezed using a roll press for uniformity of the electrode thickness. And then, the electrodes were punched to a diameter of 15 mm and the cells were assembled into 2016-coin cells in an argon-filled glove box. The amount loaded on the 15 mm diameter cathode material was approximately 4 to 5 mg. Lithium metal foil, 15 mm in diameter and 0.30 mm in thickness, was used as the counter electrode. Cellgard-2400 porous polypropylene was used as a separator. Non-aqueous 1.0 M $LiPF_6$ in EC/DMC (ethylene carbonate/dimethyl carbonate) with 1: 1 volume ratio was used as the electrolyte.

The electrochemical cycle tests were performed at ambient temperature using a galvanostatic automatic battery cycler (WonATech WBCS3000, Korea). The cells for rate test were cycled between 2.0 and 4.3 V vs. Li/Li^+ using a constant current-constant voltage (CC-CV) protocol in charging mode. The constant current rates were 0.05, 0.1, 0.2, 0.5, 1 and 2 C at 4.3 V and kept at 4.3 V until the current rate decreased to C/20 with a constant current density of 110 mAh g^{-1} for the 1 C rate. And, CV were performed at a scan rate of 0.05 mV s^{-1}.

3.4 Solid-state MAS NMR study of cathode materials

^{7}Li Magic angle spinning (MAS) nuclear magnetic resonance (NMR) measurements were carried out at room temperature on a Bruker Avance III 300 with a 7.04 T magnet. For the MAS NMR experiments, a 2.5 mm MAS probe was used with a zirconia rotor at 116.64 MHz for ^{7}Li resonance frequency. The ^{7}Li NMR spectrum was referenced to the external $LiCO_3$ powder reference. The Hahn-echo pulse sequences for ^{7}Li were used to observe the NMR signal and the sample spinning rate was 30 kHz about each ^{7}Li. The ^{7}Li spectra were acquired with a 90° pulse length of 2.0 μs, repetition delay of 0.5 s, 0.5K transients, and a spectral width of 0.60 MHz were used. The isotropic chemical shifts were successfully identified by varying the sample spinning rates (27 kHz, 30 kHz).

.

Figure 3.3 Bruker Avance III 300MHz NMR.

.

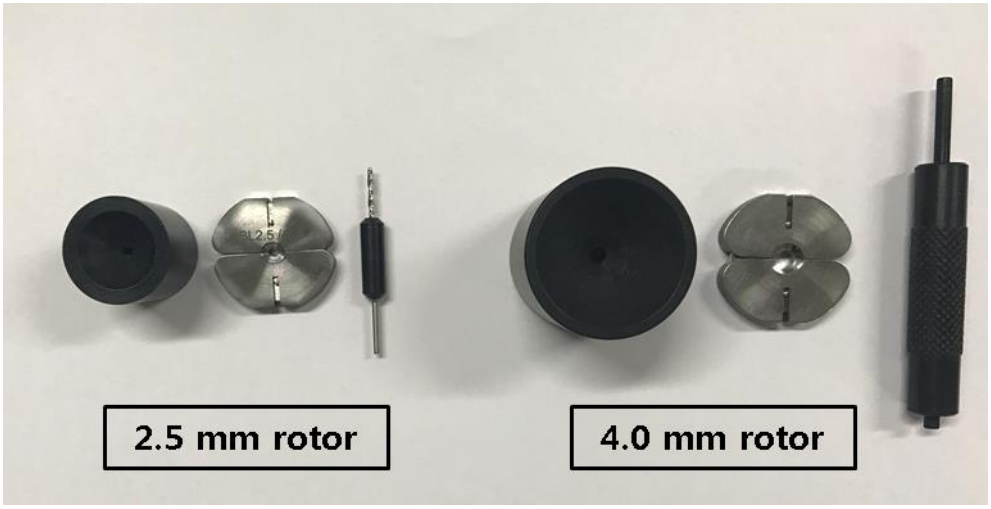

Figure 3.4 2.5 and 4.0mm sampling kit for solid-sate NMR.

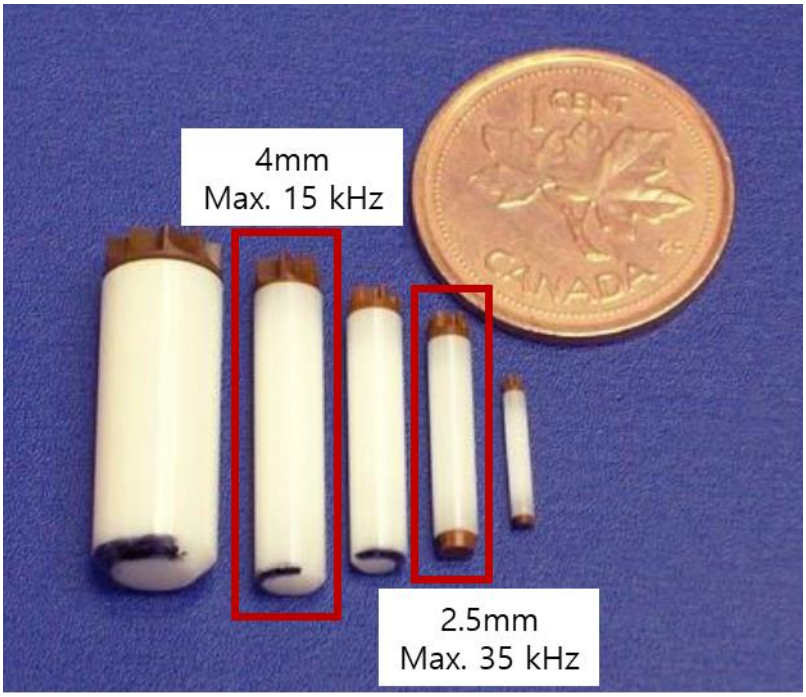

Figure 3.5 2.5 and 4.0mm solid-state NMR rotors.[35]

4. Results and Discussion

4.1 $LiFe_{1-x}Mn_xBO_3$ (x = 0, 0.25, 0.5, 0.75, 1.0)

4.1.1 X-ray Diffraction (XRD)

XRD is useful for determining the crystal structure of a solid sample by measuring the diffraction according to the angle change of the X-ray irradiating the sample. $LiFe_{0.5}Mn_{0.5}BO_3$ material has been synthesized at different sintering temperatures of 500 ℃, 550 ℃, and 600 ℃. The XRD pattern in Figure 4.1 shows the crystallization by annealing temperature. XRD data show that obtained products are monoclinic single-phase. But the aggregated peak of the sample prepared at 500 ℃ indicates that crystallization was not good. And crystallization improved as the temperature increased to 550 ℃ and 600 ℃, and there was no difference in the results between the two sintering temperatures. So the lower temperature, 550 ℃, was determined as the final sintering temperature.

The XRD pattern of $LiFe_{1-x}Mn_xBO_3$ (x = 0, 0.25, 0.5, 0.75, 1.00) compound synthesized at 550 ℃ based on the Figure 4.1. And the results are shown in Figure 4.2. The mixture has maintained a monoclinic structure. When the manganese is inserted in the structure a continuous shift of the diffraction peaks to a lower angle is observed and peak splitting has disappeared.

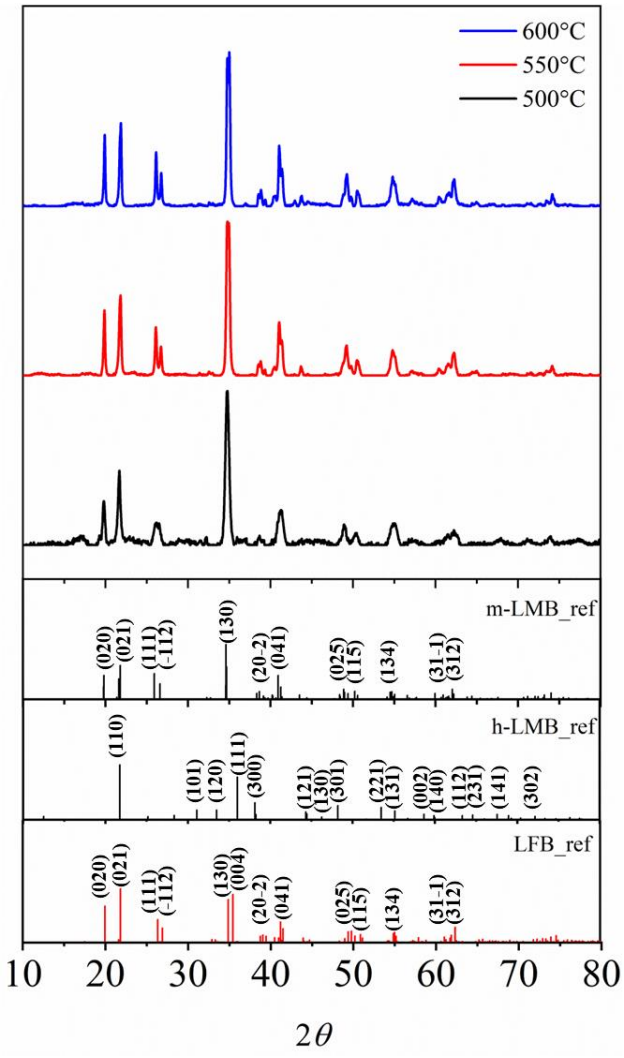

Figure 4.1 The XRD patterns of $LiFe_{0.5}Mn_{0.5}BO_3$ sintered at various temperatures.

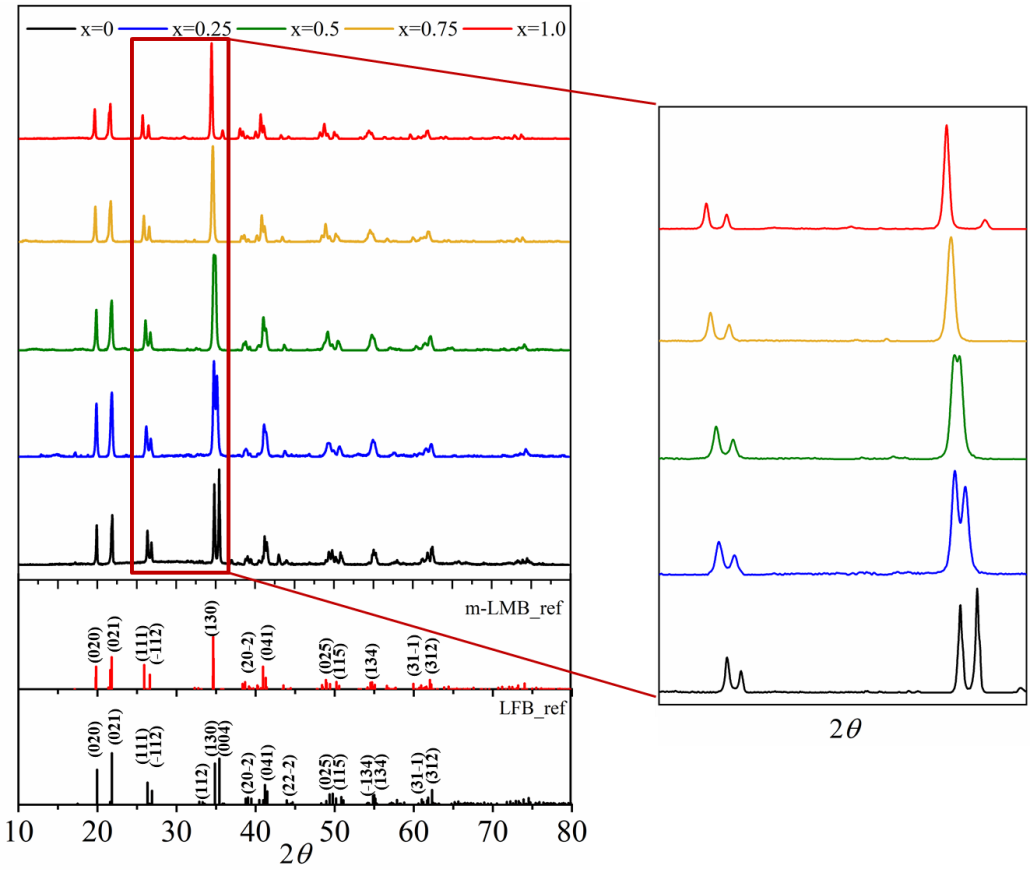

Figure 4.2 The XRD patterns of $LiFe_{1-x}Mn_xBO_3$ (x = 0, 0.25, 0.5, 0.75, 1.00) and an enlargement zone.

4.1.2 Laser-induced breakdown spectroscopy (LIBS)

This method consists from exciting and vaporizing absorbing material of any matter (in gaseous, liquid, or solid form) using a high energetic laser pulse which forms a plasma after being focused. Resulting spectral emission can be interpreted to know the composition, relative and/or absolute concentrations of atomic and even molecular forms present in the specimen. When the laser power flux is sufficiently high ionization sets in and expanding plasma is created. The goal of LIBS techniques is the search for the most favourable plasma conditions for the derivation of quantitative analytical characterization of the sample in the most different environments.[36]

The Figure 4.3 shows the enlarged wavelength bands where Fe and Mn appear. It expresses that as the ratio of Fe and Mn changes, the size of the peak changes in reverse. However, the peak intensity of Li shows that maintaining to have the same. Also, through the graph in Figure 4.4, we saw that the amounts of Fe, Mn decrease and increase quantitatively, respectively. The normalized values show the quantitative Fe and Mn, and it exists in Table 3. Figure 4.4 is plotted with the values in Table 3.

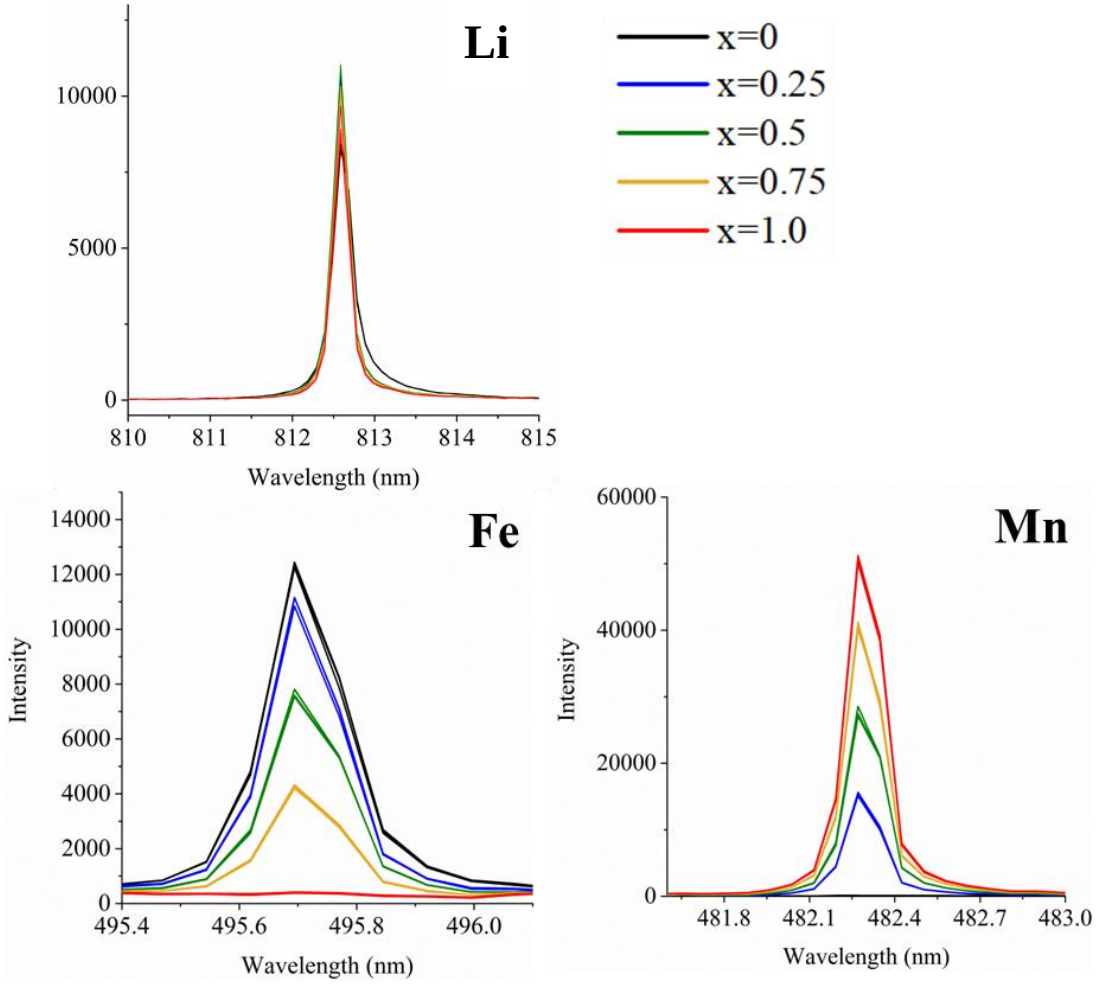

Figure 4.3 The Li, Fe and Mn LIBS data for $LiFe_{1-x}Mn_xBO_3$ (x = 0, 0.25, 0.5, 0.75, 1.00)

Table 3. Normalization data of Mn and Fe, according to *x* value.

	Mn	**Fe**
0	**0 ± 0.000194**	**1 ± 0.009705**
0.25	**0.2789 ± 0.004332**	**0.8162 ± 0.009616**
0.5	**0.5348 ± 0.006815**	**0.5492 ± 0.006155**
0.75	**0.7860 ± 0.006668**	**0.2814 ± 0.005239**
1.0	**1 ± 0.009332**	**0 ± 0.007223**

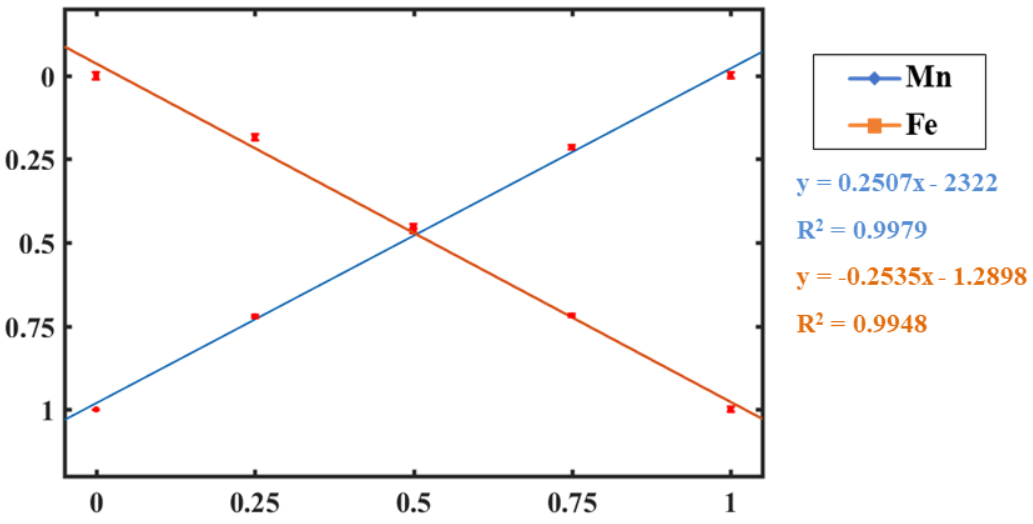

Figure 4.4 Graphical representation of Table 3.

4.1.3 ^{7}Li MAS NMR

The ^{7}Li magic angle spinning (MAS) NMR study is carried out to investigate the local environment of lithium atoms. ^{7}Li MAS NMR is a useful analytical method to investigate the local environment of lithium participating in electrochemical reactions in cathode materials. This measurements were used to compare the chemical shift of $LiFe_{1-x}Mn_xBO_3$ (x = 0, 0.25, 0.5, 0.75, 1.0) according to the iron and manganese ratio. The isotropic peaks are pointed out by asterisks (*) and other peaks are spinning side bands. As shown in Figure 4.5, all materials shows a single isotropic peak and none mixture materials, $LiFeBO_3$ and $LiMnBO_3$, isotropic peaks appear at -232.9, -192.7 ppm, respectively. These peaks are well-matched with previously reported ^{7}Li MAS NMR data.[17, 20] Isotropic peaks are shifted to downfield, when the amount of manganese increased because manganese has one less electron at e" state compared with iron (Figure 4.7). The position of the peak is shown in Table 4. The peak positions were plotted as shown in Figure 4.6, and the linear fitting equation was calculated as $y = 38.04x - 236.24$ with the coefficient of correlation (R^2) 0.9217.

Lithium metal borate materials have two close positions for lithium and one position for transition metal (“2Li 1M”).[14, 37] So ^{7}Li MAS NMR data show relatively broad peaks and $LiMnBO_3$ has two isotropic peaks.

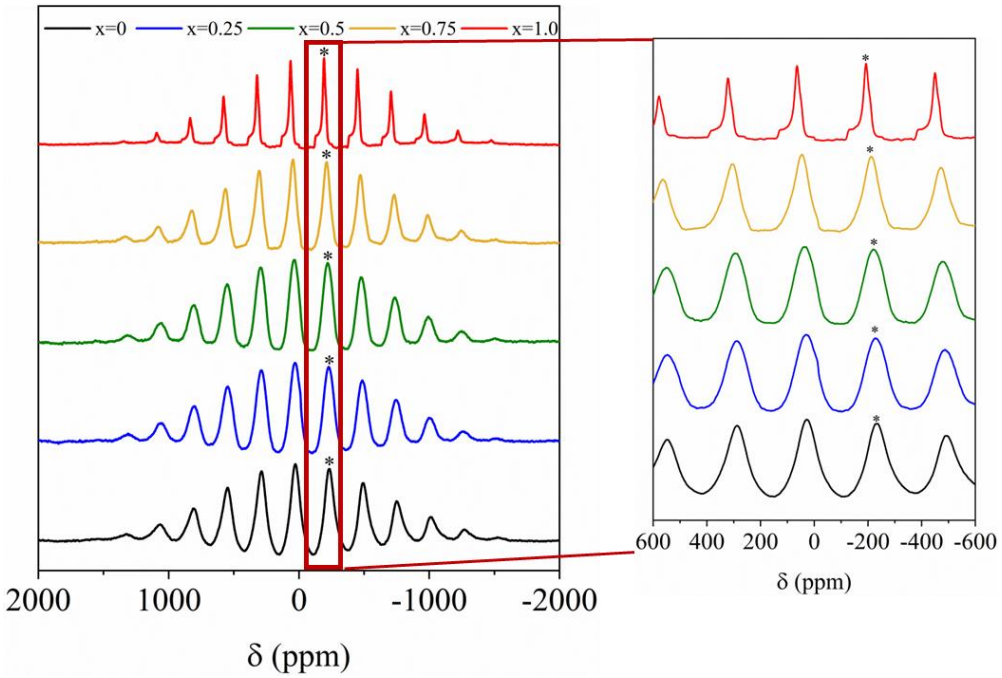

Figure 4.5 ^{7}Li MAS NMR spectra of $LiFe_{1-x}Mn_xBO_3$ at sample spinning rate of 30kHz. The isotropic peaks are indicated by asterisk(*).

Table 4. Isotropic peak positions of the $LiFe_{1-x}Mn_xBO_3$.

x	ppm
1.0	**-192.7**
0.75	**-212.8**
0.5	**-220.2**
0.25	**-227.5**
0	**-232.9**

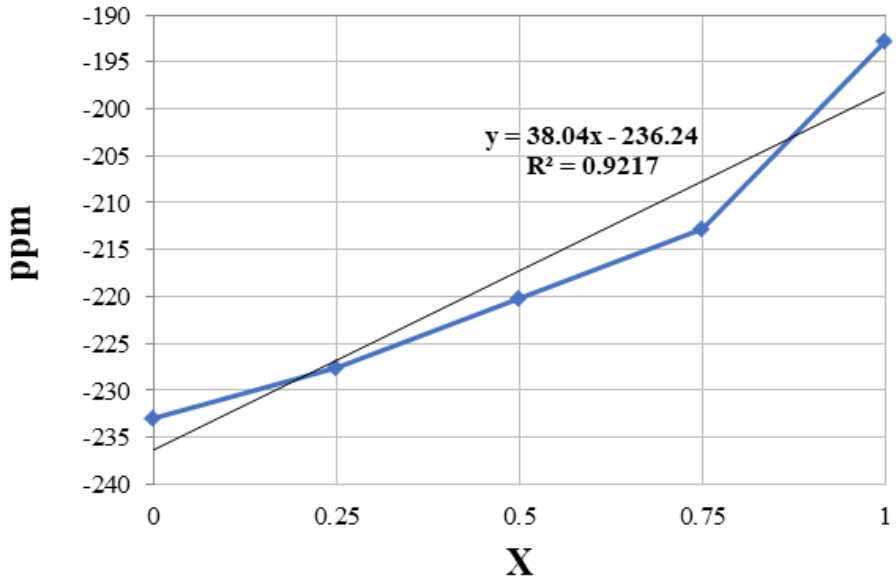

Figure 4.6 Graphical representation of Table 4 with linear fitting equation and coefficient of correlation.

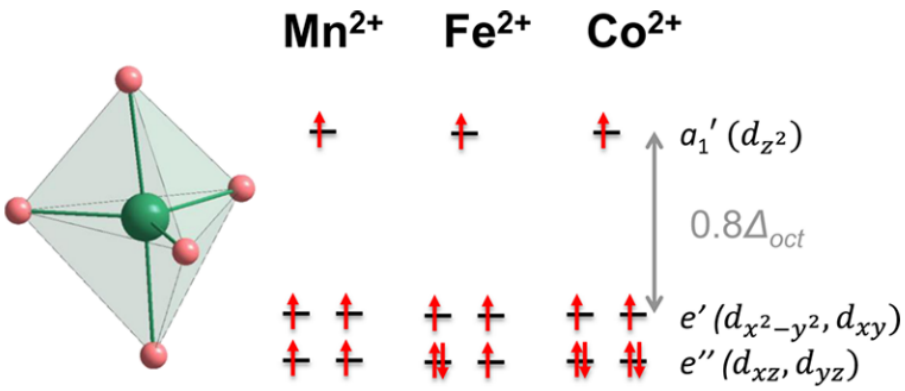

Figure 4.7 Proposed energy splitting and filling of the trigonal bipyramidal crystal fields (e″, e′, and a_1').[14]

4.1.4 Electrochemical study

The cycling performance of $LiFe_{1-x}Mn_xBO_3$ (x=0, 0.25, 0.5, 0.75 and 1.0) at 0.5C are shown in Figure 4.8. The highest capacity was seen when x was 0.25, but it increased gradually. This phenomenon may occur when the resistance of the material is high. Next, when x is 0.5, the capacity was higher than that of LFB, but it was confirmed that capacity fading was large. Through this, it was confirmed that when a mixture of fe and mn was used, the capacity was higher than when it was not. When x is 0.25, the capacity fading occurs, but it is not severe and after cyclying it shows a higher capacity than LFB.

The rate performance of $LiFe_{1-x}Mn_xBO_3$ (x=0, 0.25, 0.5, 0.75 and 1.0) are shown in Figure 4.9. The cells were cycled at 0.05, 0.1, 0.5, 1.0, and 2.0 C in the voltage range of 1.0 – 4.5 V. The discharge capacities of all the samples decreased with increasing current density. As can be seen from the data, when x is 0.25 and 0.5, the capacity is higher than that of LFB at low C-rates. However, 0.5 represents a lower capacity than LFB from 0.5 C. And x=0.25 gives a higher capacity even at a high c-rate. So, it was confirmed that when the mixture was made of iron and manganese, it had a higher capacity than LFB and LMB, and the electrochemical performance as a cathode material was improved.

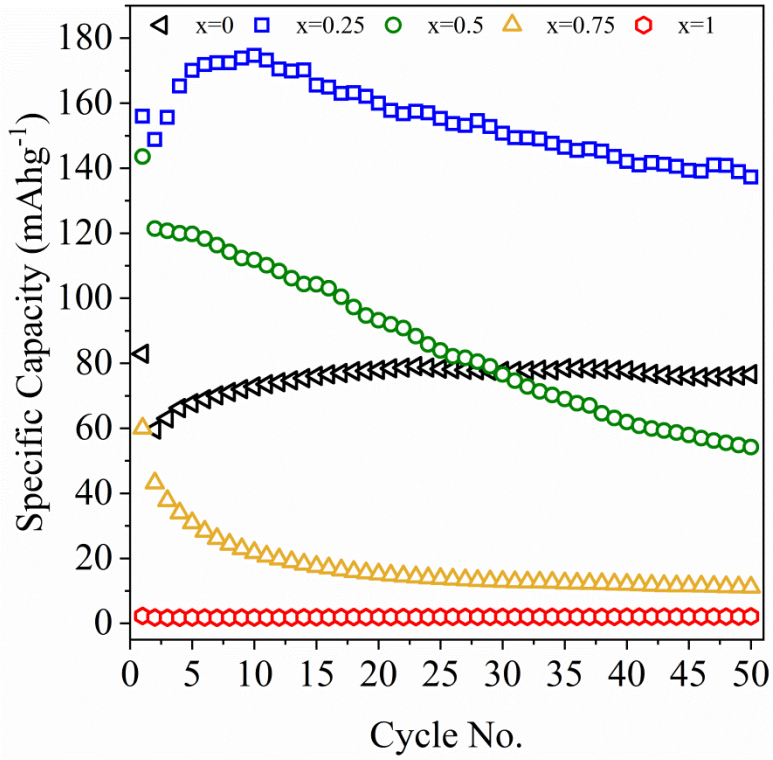

Figure 4.8 The long cycle ability at 0.5C of $LiFe_{1-x}Mn_xBO_3$ series.

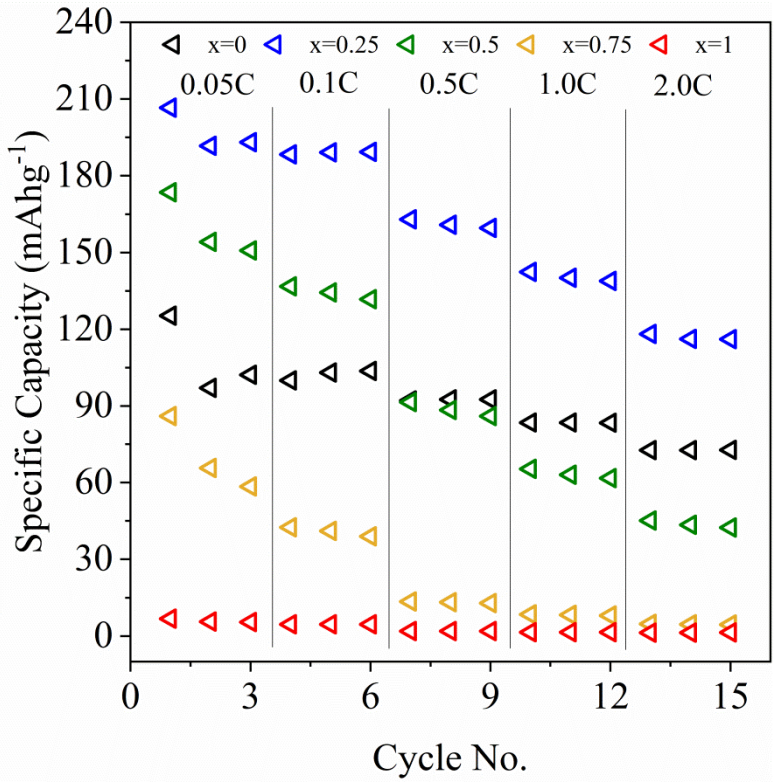

Figure 4.9 The rate performance at various C-rate of $LiFe_{1-x}Mn_xBO_3$ series.

4.2 $LiFe_{1-x}Co_xBO_3$ (x = 0, 0.25, 0.5, 0.75, 1.0)

4.2.1 X-ray Diffraction (XRD)

To determine the crystal structure $LiFe_{1-x}Co_xBO_3$ XRD analysis was performed. In order to obtain a material with the best crystal structure, synthesis was performed at various temperatures of 500 ℃, 530 ℃, 600 ℃ then XRD was measured. Unlike $LiFe_{1-x}Mn_xBO_3$, $LiFe_{0.75}Co_{0.25}BO_3$ was synthesis at 530 ℃ becasue XRD pattern showed a very high metal Co XRD peak intensity near 36° when the synthesis was performed at 600 ℃. So a temperature, which is suitable for synthesis of $LiCoBO_3$, close to 500 ℃ was selected.[38] The final synthesis temperature was selected as 530 ℃. On the other hand, XRD patterns of products synthesized at 500 ℃ showed aggregated peaks at 25° and 50° which indicate a bad crystallinity. These results indicates that at low temperaturesFe cannot form crystal structure. Excluding the metal peaks which is formed in all temperatures a monoclinic structure well matched with references can be concluded (Figure 4.8).

The XRD pattern of $LiFe_{1-x}Co_xBO_3$ (x = 0, 0.25, 0.5, 0.75, 1.00) compound synthesized at 530 ℃ is shown in Figure 4.9. The mixtures have maintained a monoclinic structure but metal peaks still appear near 42 - 45° which are indicated with asterisk(*).When the cobalt is inserted in the structure, a continuous shift of the diffraction peaks to a higher angle is observed.

Because of the presence of metal impurity peaks, LIBS measurement for quantitative analysis was not performed.

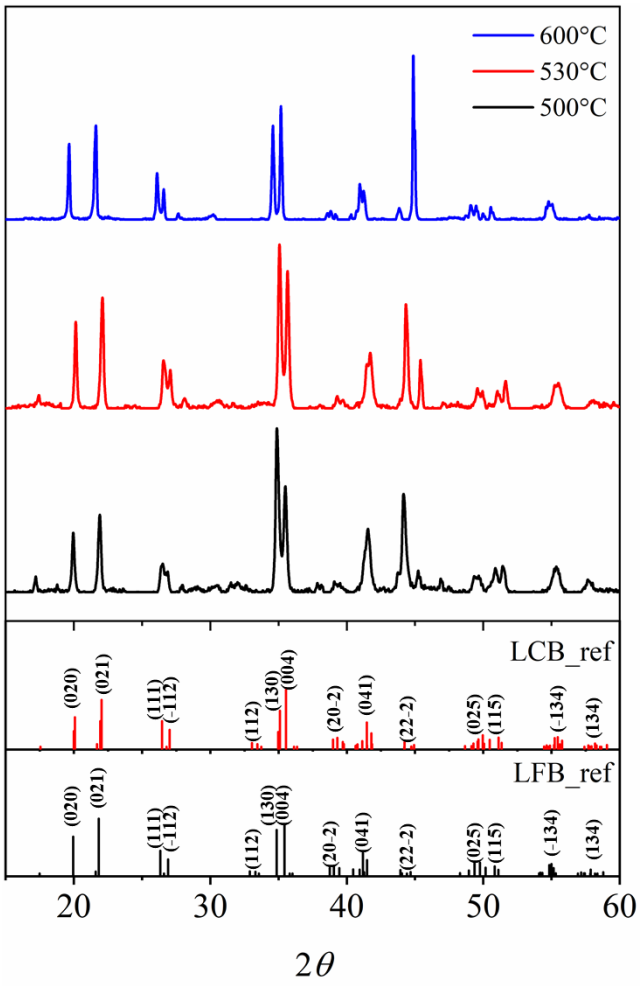

Figure 4.10 The XRD patterns of $LiFe_{0.75}Co_{0.25}BO_3$ sintered at various temperatures.

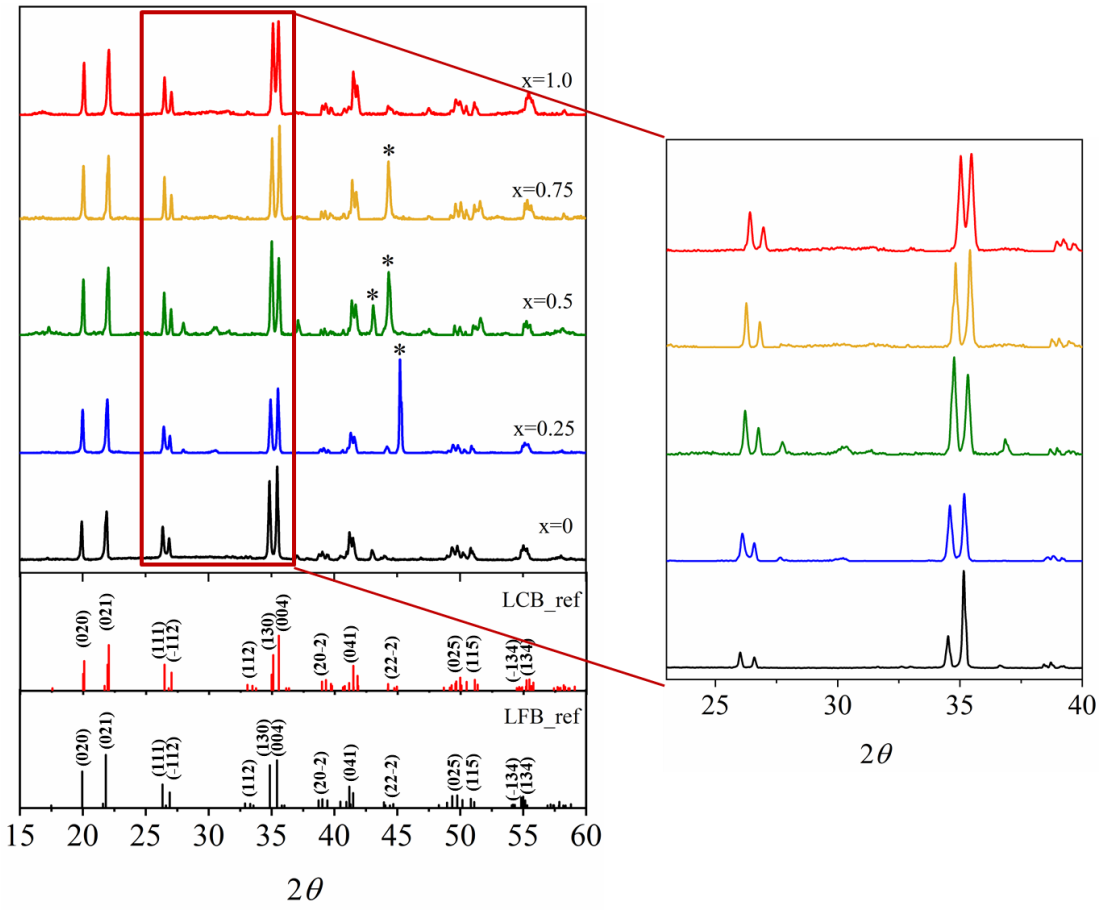

Figure 4.11 The XRD patterns of $LiFe_{1-x}Co_xBO_3$ (x = 0, 0.25, 0.5, 0.75, 1.00) and an enlargement zone. The impurities are indicated by asterisk(*).

4.2.3 ^{7}Li MAS NMR

The ^{7}Li magic angle spinning (MAS) NMR is measured to investigate the local environment of lithium atoms for $LiFe_{1-x}Co_xBO_3$ (x = 0, 0.25, 0.5, 0.75, 1.0). The isotropic peaks are pointed out by asterisks (*) and other peaks are spinning side bands. As shown in Figure 4.10, none mixture materials, $LiFeBO_3$ and $LiCoBO_3$, isotropic peaks appear at -232.9, -57.1 ppm, respectively.[17, 39] These peaks are well-matched with its previous ^{7}Li MAS NMR data. The cobalt has one more electron at e" state compared with iron (Figure 4.7), so isotropic peaks are shifted to upfield, when the amount of cobalt increasedas shown in Table 5.

The ^{7}Li NMR spectrum of $LiCoBO_3$ is significantly broadened by the dipolar interactions between Li and the unpaired electrons associated with Co^{2+}.[39] The smaller shift of $LiCoBO_3$ is almost certainly a result of the smaller spin of Co^{2+} compare to that of Fe^{2+} (Co^{2+}: S = 3/2, Fe^{2+}: S = 2). The extra d-electron in this ion results in fewer unpaired electrons within the trigonal-bipyramidal ligand environment.

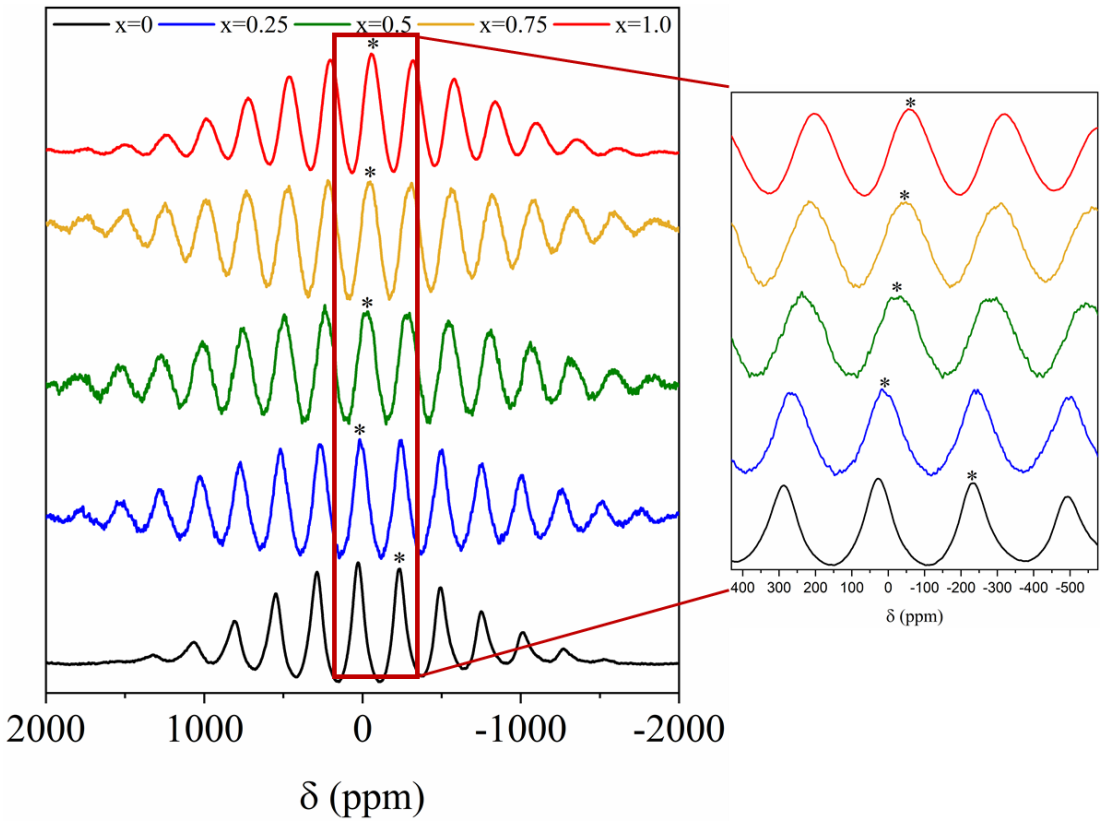

Figure 4.12 ^{7}Li MAS NMR spectra of $LiFe_{1-x}Co_xBO_3$ at sample spinning rate of 30 kHz. The isotropic peaks are indicated by asterisk(*).

Table 5. Isotropic peak positions of the $LiFe_{1-x}Co_xBO_3$.

x	ppm
1.0	**-57.1**
0.75	**-43.9**
0.5	**-26.4**
0.25	**-22.7**
0	**-232.9**

5. Conclusion

The $LiFe_{1-x}Mn_xBO_3$ and $LiFe_{1-x}Co_xBO_3$ cathode material, which is a complex material of Mn, Fe, and Co, used for the lithium-ion battery were synthesized by the solid-state reaction. Different analytical techniques such as XRD, LIBS, and Solid-state NMR were used for enhanced structural characterization and quantitative analysis. Synthesized materials were sintering at various temperatures, and according to the measured XRD result, the sintering temperature was optimized as 550 ℃ ($LiFe_{1-x}Mn_xBO_3$) and 530 ℃ ($LiFe_{1-x}Co_xBO_3$). In the case of $LiFe_{1-x}Mn_xBO_3$, LIBS was measured for the quantitative analysis of metals in the samples, and the result was consistent with the desired ratio. At $LiFe_{1-x}Co_xBO_3$, since a metal impurity peak appeared in XRD, quantitative analysis was not performed. Solid-state MAS NMR was measured in order to perform structural analysis through ^7Li nucleus. In energy level splitting for $LiMBO_3$, the number of electrons increases by one in the order of Mn, Fe, and Co in the e" state. As a result, it shows that isotropic peaks are shifted to up-field as the number of electrons increases. And $LiMBO_3$ have broad isotropic peaks than other materials because they have two positions for lithium (“2Li 1M”).

6. References

1. Heide Budde-Meiwes, J. D., Benedikt Lunz, Jens Muennix, Susanne Rothgang, Julia Kowal and Dirk Uwe Sauer, A review of current automotive battery technology and future prospects. *J Automobile Engineering* **2013,** *227* (5), 761-776.
2. Ozawa, K., Lithium-ion rechargeable batteries with $LiCoO_2$ and carbon electrodes: the $LiCoO_2$/C system. *Solid State Ionics* **1994,** *69* (3), 212-221.
3. Whittingham, M. S., Lithium Batteries and Cathode Materials. *Chemical Reviews* **2004,** *104* (10), 4271-4302.
4. Micromeritics Instrument Corporation. Zeta Potential Analysis of Lithium Ion Battery Electrolytes. AZoM. . **October 12, 2020**.
5. Roy, P.; Srivastava, S. K., Nanostructured anode materials for lithium ion batteries. *Journal of Materials Chemistry A* **2015,** *3* (6), 2454-2484.
6. Picciotto, M. M. T. J. J. A. d., Electrochemical extraction of lithium from $LiMn_2O_4$. *Materials Research Bulletin* **1984,** *19* (2), 179-187.
7. Fergus, J. W., Recent developments in cathode materials for lithium ion batteries. *Journal of Power Sources* **2010,** *195* (4), 939-954.
8. Yang, Z. G. a. Y., Recent advances in the research of polyanion-type cathode materials for Li-ion batteries. *Energy & Environmental Science* **2011,** *4* (9), 3223-3242.
9. Christian M. Julien, A. M., Karim Zaghib and Henri Groult Comparative Issues of Cathode Materials for Li-Ion Batteries. *inorganics* **2014,** *2* (1), 132-154.
10. Dong-Hwa Seo, Young-Uk Park, Sung-Wook Kim, Inchul Park, R. A. Shakoor, and Kisuk Kang, First-principles study on lithium metal borate cathodes for lithium rechargeable batteries. *PHYSICAL REVIEW B* **2011,** *83*.
11. V. Legagneur, Y. A., A. Mosbah, R. Portal, A. Le Gal La Salle, A. Verbaere, D. Guyomard,

Y. Piffard, $LiMBO_3$ (M=Mn, Fe, Co): synthesis, crystal structure and lithium deinsertion / insertion properties. *Solid State Ionics* **2001,** *139*, 37-46.

12. Veena Ragupathi, S. K., Sudarkodi Raman, Puspamitra Panigrahi, Juwon Lee, Ganapathi Subramaniam Nagarajan∗, Enhanced electrochemical performance of $LiCoBO_3$ cathode material for next generation Lithium-ion batteries. *Applied Surface Science* **2018,** *449*, 421–425.
13. Prabeer Barpanda, D. D., Swatilekha Ghosh, Yongho Kee, Shigeto Okada, Lithium metal borate ($LiMBO_3$) family of insertion materials for Li-ion batteries: a sneak peak. *Ionics* **2015,** *21*, 1801-1812.
14. Liang Tao, J. R. N., Brent C. Melot,Tyrel M. McQueen,Christian Masquelier,and Gwenaëlle Rousse*, Magnetic Structures of $LiMBO_3$ (M = Mn, Fe, Co) Lithiated Transition Metal Borates. *Inorganic Chemistry* **2013,** *52*, 11966-11974.
15. Atsuo Yamada, N. I., Yu Harada, Shin-ichi Nishimura, Yukinori Koyama, Isao Tanaka, Lithium Iron Borates as High-Capacity Battery Electrodes. *Advanced Materials* **2010,** *22* (32), 3583–3587.
16. Y.Z. Dong, Y. M. Z., Z.D. Shi, X.N. An, P. Fu, L. Chen, The structure and electrochemical performance of $LiFeBO_3$ as a novel Li-battery cathode material. *Electrochimica Acta* **2008,** *53* (5), 2339-2345.
17. Shou-Hang Bo, F. W., Yuri Janssen, Dongli Zeng, Kyung-Wan Nam, Wenqian Xu, Lin-Shu Du, Jason Graetz, Xiao-Qing Yang, Yimei Zhu, John B. Parise, Clare P. Grey* and Peter G. Khalifah*, Degradation and (de)lithiation processes in the high capacity battery material $LiFeBO_3$. *journal of Materials Chemistry* **2012,** *22*.
18. Jae Chul Kim, C. J. M., Byoungwoo Kang, Geoffroy Hautier, Anubhav Jain,and Gerbrand Ceder, Synthesis and Electrochemical Properties of Monoclinic $LiMnBO_3$ as a

Li Intercalation Material. *Journal of The Electrochemical Society* **2011,** *158* (3), A309-A315.

19. Y.-S. Leea and H. Leeb, Electrochemical properties of $LiMnBO_3$ as a potential cathode material for lithium batteries. *Journal of Ceramic Processing Research* **2012,** *13*, s237~s240.
20. Jae Chul Kim, X. L., Charles J. Moore, Shou-Hang Bo, Peter G. Khalifah, Clare P. Grey, and Gerbrand Ceder*, Analysis of Charged State Stability for Monoclinic $LiMnBO_3$ Cathode. *chemistry of materials* **2014,** *26*, 4200−4206.
21. Atsuo Yamada*, N. I., Shin-ichi Nishimura, Yukinori Koyama and Isao Tanaka, Synthesis and electrochemistry of monoclinic $Li(Mn_xFe_{1-x})BO_3$: a combined experimental and computational study. *journal of Materials Chemistry* **2011,** *21*.
22. Anping Tang, Q. Z., Guorong Xu and Haishen Song Spherical $LiCoBO_3$ particles prepared via a molten salt method for lithium ion batteries. *RSC Advances* **2016,** *6* (87), 4439-84444.
23. Yasunobu Yamashita, P. B., Yuki Yamada, and Atsuo Yamada∗, Demonstration of Co^{3+}/Co^{2+} Electrochemical Activity in $LiCoBO_3$ Cathode at 4.0 V. *Electrochemistry Letters* **2013,** *2* (8), A75-A77.
24. Robinson, J. W., Undergruaduate Instrumental Analysis *CRC Process* **2005**.
25. http://hiq.linde-gas.com/en/analytical_methods/nuclear_magnetic_resonance.html.
26. Maciejewski, M., Basics of NMR Spectroscopy. **2016**.
27. Oliver Pecher, J. C.-G., Kent J. Griffith, and Clare P. Grey, Materials' Methods: NMR in Battery Research. *Chemistry of Materials* **2016,** *29*, 213-242.
28. http://mriquestions.com/predict-nuclear-spin-i.html.
29. Edward, J. C., Pricnicple of NMR. **2009,** *87A*.

30. Ridgway, J. P., Cardiovascular magnetic resonance physics for clinicians: part I. *Journal of Cardiovascular Magnetic Resonance* **2010,** *12* (1), 71.

31. Schurko, R., Introduction to Solid State NMR. **2002**, 1-30.

32. A. Alia, S. G., Huub J. M. de Groot, Magic angle spinning(MAS) NMR: a new tool to study the spatial and electronic structure of photosynthetic complexes. *Photosynthesis reserch* **2009,** *102* (2), 415-425.

33. Mikheil Gogiashvili 1, Jessica Nowacki 1, Roland Hergenröder 1 , Jan G. Hengstler 2 , Jörg Lambert 1,† and Karolina Edlund 2, HR-MAS NMR Based Quantitative Metabolomics in Breast Cancer. *Metabolites* **2019,** *9* (2), 19.

34. Polenova, T., Spinning into focus. *Nature Chemistry* **2011,** *3*.

35.http://u-of-o-nmr-facility.blogspot.com/2008/04/how-much-sample-do-i-need-to-get-solid.html.

36. Malvezzi, A. M., Laser–Matter Interaction in LIBS Experiments. *Laser-Induced Breakdown Spectroscopy* **2014,** *182*, 3-29.

37. L. Tao, G. R., J.N. Chotard, L. Dupont, S. Bruyère, D. Hanžel, G. Mali, R. Dominko, S. Levasseur & C. Masquelier*, Preparation, Structure and Electrochemistry of $LiFeBO_3$: a Cathode Material for Li-ion Battery. *Journal of Materials Chemistry A* **2014,** (7), 2060-2070.

38. Barbara Le Roux, C. B., Oleg I. Lebedev, Jean-François Colin, and Valerie Pralong, Synthesis and Characterization of the $LiMnBO_3$–$LiCoBO_3$ Solid Solution and Its Use as a Lithium-Ion Cathode Material. *Inorganic Chemistry* **2015,** *54*, 5273-5279.

39. Shou-Hang Bo, G. M. V., Michael R. Saccomanno, Huafeng Huang, Polina V. Burmistrova,Andrew C. Malingowski, Robert L. Sacci, Kevin R. Kittilstved, Clare P. Grey, and Peter G. Khalifah*, Thin-Film and Bulk Investigations of $LiCoBO_3$ as a Li-Ion

Battery Cathode. *Applied materials interfaces* **2014,** *6*, 10840−10848.